Iron isotope behavior during fluid/rock interaction in K-feldspar alteration zone – A model for pyrite in gold deposits from the Jiaodong Peninsula, East China

Zhi-Yong Zhu [a,b], Shao-Yong Jiang [c,*], Ryan Mathur [d], Nigel J. Cook [b],
Tao Yang [a], Meng Wang [e], Liang Ma [f], Cristiana L. Ciobanu [b]

[a] State Key Laboratory for Mineral Deposits Research, School of Earth Sciences and Engineering,
Nanjing University, Nanjing 210093, Jiangsu, China
[b] School of Chemical Engineering, The University of Adelaide, Adelaide, SA 5005, Australia
[c] State Key Laboratory of Geological Processes and Mineral Resources, Collaborative Innovation Center for
Exploration of Strategic Mineral Resources, Faculty of Earth Resources, China University of Geosciences, Wuhan 430074, Hubei, China
[d] Department of Geology, Juniata College, Huntingdon, PA 16652, USA
[e] School of the Environment, Nanjing University, Nanjing 210093, Jiangsu, China
[f] Guangzhou Institute of Geochemistry, Chinese Academy of Sciences, Guangzhou 510640, Guangdong, China

Received 24 October 2016; accepted in revised form 1 October 2017; available online 12 October 2017

Abstract

Mechanisms for Fe isotope fractionation in hydrothermal mineral deposits and in zones of associated K-feldspar alteration remain poorly constrained. We have analyzed a suite of bulk samples consisting of granite displaying K-feldspar alteration, Precambrian metamorphic rocks, and pyrite from gold deposits of the Jiaodong Peninsula, East China, by multi-collector inductively-coupled plasma mass spectrometry. Pyrites from disseminated (J-type) ores show a $\delta^{56}Fe$ variation from $+0.01$ to $+0.64‰$, overlapping with the signature of the host granites ($+0.08$ to $+0.39‰$). In contrast, pyrites from quartz veins (L-type ores) show a wide range of Fe-isotopic composition from -0.78 to $+0.79‰$. Negative values are never seen in the J-type pyrites. The Fe isotope signature of the host granite with K-feldspar alteration is significantly heavier than that of the bulk silicate Earth. The Fe isotopic compositions of Precambrian metamorphic rocks across the district display a narrow range between $-0.16‰$ and $+0.19‰$, which is similar to most terrestrial rocks. Concentrations of major and trace elements in bulk samples were also determined, so as to evaluate any correlation between Fe isotope composition and degree of alteration. We note that during progressive K-feldspar alteration to rocks containing >70 wt% SiO_2, >75 ppm Rb, and <1.2 wt% total Fe_2O_3, the Fe isotope composition of the granite changes systematically. The Fe isotope signature becomes heavier as the degree of alteration increases. The extremely light Fe isotopic compositions in L-type gold deposits may be explained by Rayleigh fractionation during pyrite precipitation in an open fracture system. We note that the sulfur isotopic compositions of pyrite in the two types of ores are also different. Pyrite from J-type ores has a systematically 3.5‰-higher $\delta^{34}S$ value (11.2‰) than those of pyrite from the L-type ores (7.7‰). There is, however, no correlation between Fe and S isotope signatures. The isotopic fractionation of sulfur is used to constrain a change in the fO_2 of the hydrothermal fluids from which pyrite precipitated.

This work demonstrates that the Fe isotope composition of pyrite displays a significant response to the process of pyrite precipitation in hydrothermal systems, and that systematic fractionation of iron isotopes occurs during fluid/rock reaction in the K-feldspar alteration zone of the Linglong granite. The implications of the results are that processes of mineralization and

* Corresponding author at: State Key Laboratory of Geological Processes and Mineral Resources, China University of Geosciences, Wuhan, China.
E-mail address: shyjiang@cug.edu.cn (S.-Y. Jiang).

associated fluid-rock interaction, which are ubiquitously observed in porphyry-style Cu-Au-Mo and other hydrothermal deposits, may be readily traceable using Fe isotopes.

1. INTRODUCTION

Recent advances in multi-collector inductively coupled plasma mass spectrometry (MC-ICP-MS) allow for accurate and precise measurement of transition metal isotopes. Direct analysis of the stable isotope ratios of the metals themselves (e.g., Cu, Fe, or Zn) provides a potential new tool to constrain ore-forming process, and may also have applications in exploration for hidden deposits (Zhu et al., 2000; Mathur et al., 2009; Li et al., 2010; Wawryk and Foden, 2015). In comparison with the relatively large datasets for Cu isotopes in hydrothermal ore deposits (Graham et al., 2004; Maher and Larson, 2007; Mathur et al., 2009; Li et al., 2010), Fe isotopes in hydrothermal deposits are less well studied, and the mechanisms of Fe isotope fractionation remain disputed (Sharma et al., 2001; Johnson et al., 2003; Beard et al., 2003a, 2003b; Blanchard et al., 2009; Guilbaud et al., 2011). Nevertheless, several studies of Fe isotope systematics in ore deposits, notably in skarns (Graham et al., 2004; Wang et al., 2011, 2015; Wawryk and Foden, 2015; Zhu et al., 2016), in porphyry Cu deposits (Graham et al., 2004; Li et al., 2010), as well as in low- to moderate-temperature hydrothermal deposits (Markl et al., 2006; Gagnevin et al., 2012; Gao et al., 2017) have contributed to a fundamental understanding of Fe isotope behavior and fractionation in hydrothermal systems. Unlike other metal stable isotopes (e.g. Cu and Zn), Fe is a major element in the Earth's crust, meaning that Fe isotopes have only weak significance for tracing metal source. However, precisely because of the widespread distribution of Fe-bearing minerals in ore deposits, Fe-isotopes represent a potential tool for interpretation of ore-forming processes.

Here, we address the Fe isotope signatures of pyrite from gold deposits in order to constrain Fe isotope fractionation behavior associated with alteration and mineralization. Giant gold deposits hosted in granites from the Jiaodong Peninsula, East China, are of two main types, vein and disseminations (Fig. 1; Lü and Kong, 1993). They both belong to the orogenic class of gold deposits (Groves et al., 1998; Goldfarb et al., 2001; Chen, 2006; Jiang et al., 2009), occur within the same metallogenic system, and are broadly similar in geology, geochronology and geochemistry. The well-documented geological settings of these deposits and the good constraints on the composition and physical–chemical parameters of the ore-forming fluids make them a natural laboratory amenable to study fractionation mechanisms of Fe isotopes in the hydrothermal environment.

To achieve these goals, a systematic study of Fe- and S-isotopes was conducted on pyrite from the two types of hydrothermal gold deposits from the Jiaodong Peninsula, as well as the behavior of Fe isotopes of fluid/rock interaction in K-feldspar altered granite for which whole rock major and trace element data are available. The demonstrated variations in Fe isotope behavior in mineralization and K-feldspar alteration provide new constraints on ore-forming processes. In doing so, we aim to demonstrate Fe isotope behavior during water–rock interaction associated with K-feldspar alteration, shed new light on the source of metals in the deposits, and constrain the ore-forming processes involved.

2. BACKGROUND ON FE ISOTOPES AND THEIR FRACTIONATION TRENDS

Previous studies of Fe-isotopic variation in igneous rocks have mostly focused on fresh bulk samples, including I-, A-, and S-type granite, basalts, as well as mafic–ultramafic intrusive rocks (e.g., Beard et al., 2003b; Wang et al., 2012; Chen et al., 2013; Foden et al., 2015; Bilenker et al., 2017). Whereas there is consensus on heavy Fe isotopes being typical of highly evolved magmas, there are differences in interpreting such observations. For example, late magmatic aqueous fluids exsolved from granitic magmas are considered to preferentially remove the lighter isotopes of iron, thus leaving the residual magma enriched in the heavier isotopes (Poitrasson and Freydier, 2005; Heimann et al., 2008). In contrast, mechanisms intrinsic to magmatic evolution such as fractional crystallization, could instead be responsible for the same trends since early formed minerals containing Fe such as olivine or titanomagnetite are shown to concentrate lighter Fe isotopes (Teng et al., 2008; Schuessler et al., 2009).

The proportion of Fe^{3+} in the total iron budget of a magma depends on oxygen fugacity (fO_2), and iron isotopes therefore act as effective probes of the redox state of terrestrial magmas, and by implication, also their tectonic settings (Sossi et al., 2012). In contrast, granites, notably those recording K-feldspar alteration, a widespread style of alteration related to hydrothermal ore-forming process (Ulrich and Heinrich, 2002), have attracted little prior attention. Such rocks can, in some cases, have significantly different Fe isotope signatures from terrestrial igneous rocks, prompting the question of whether Fe isotopes could be systematically applied as a tool in mineral exploration.

Several studies have dealt with Fe-isotope measurements of active seafloor hydrothermal systems. For example, on the Juan de Fuca Ridge, Fe isotope values from vent fluids are lighter compared with associated basalts and precipitated sulfides (Sharma et al., 2001), suggesting that vent fluids may have provided a source of light Fe isotopes to the deep oceans. Hot fluids from mid-ocean-ridge settings also show a lighter Fe isotopic signature compared to igneous
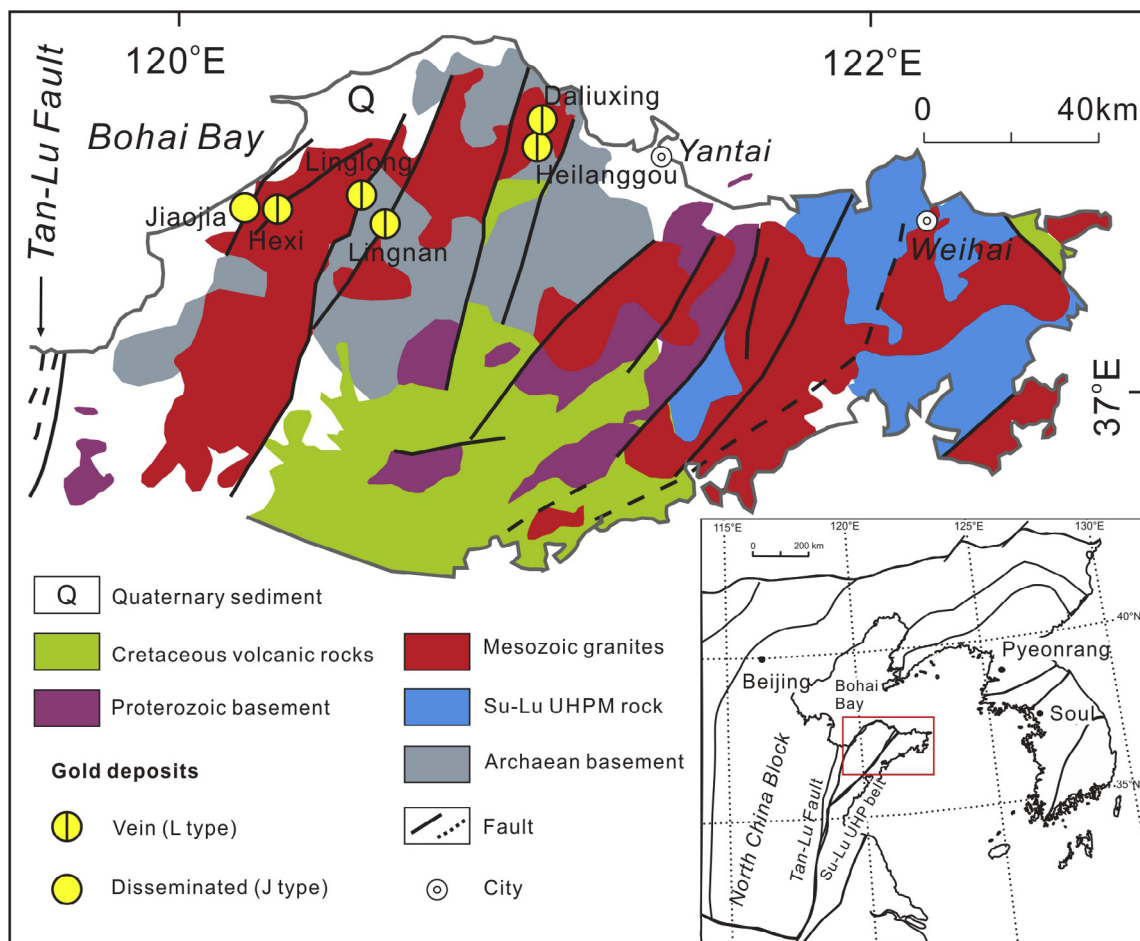
Fig. 1. Simplified geological map showing the locations of sampled gold deposits and faults in the Jiaodong gold province (modified from Tang et al., 2007). UHPM – Ultra High Pressure Metamorphic.

rocks (Beard et al., 2003a). The hydrothermal fluid can certainly supply the light Fe isotope but it is difficult to readily explain the significant differences in the Fe isotope signatures of pyrite in the two kinds of deposits in this study given that they belong to the same metallogenic system. Might this difference provide any information that can be linked to the ore forming process? Iron and S are the two main constituents of pyrite and both are sensitive to the redox conditions. Studies of Fe-S isotopes in hydrothermal fluids related to active seafloor sulfide deposits from the East Pacific Rise (Rouxel et al., 2008) suggest that pyrite retains the effects of a strong kinetic Fe-isotope fractionation during iron sulfide precipitation. A remarkable co-variation of Fe and S isotopes was observed in the Archean microbial reduction process (Archer and Vance, 2006). This prompts the question of whether there is any systematic relationship between Fe and S isotopes in hydrothermal ore deposits?

Important for understanding Fe isotope systematics in mineralizing systems is the fractionation between Fe-minerals and fluid relative to temperature. There is a substantial body of published experimental measurements or theoretical calculations on mineral–fluid pairs. Despite the large number of attempts aimed at constraining Fe isotope fractionation factors, results and interpretations are sometimes inconsistent. Examining each of the factors potentially inducing fractionation is necessary before quantitatively discussing the fractionation behavior in the ore-forming systems such as those studied here or elsewhere.

The theoretical fractionation between aqueous Fe^{3+} and Fe^{2+} species has been studied (Schauble et al., 2001; Anbar et al., 2005), and these theoretical estimations are concordant with experimental results (Johnson et al., 2002; Welch et al., 2003). Theoretical calculations of fractionation among solid species, such as siderite (Blanchard et al., 2009), goethite (Polyakov and Mineev, 2000), and hematite (Polyakov et al., 2007; Blanchard et al., 2009), also agree well with experimental studies (Beard et al., 2010). However, Beard et al. (2010) found a serious inconsistency between experimental and theoretical fluid-mineral fractionation factors when combining β-factors for aqueous Fe species and solids. Rustad et al. (2010) proposed an improved calculation for aqueous Fe complexes, where a second water shell was embedded into the previously used aqueous species, $Fe(H_2O)_6^{3+}$ and $Fe(H_2O)_6^{2+}$ (Schauble et al., 2001; Anbar et al., 2005), even taking the third water shell effect into account. The β-factors for aqueous Fe^{3+}

and Fe^{2+} species derived from Mössbauer spectroscopy (Polyakov and Soultanov, 2011) are in an excellent agreement with the modified calculation of Rustad et al. (2010). Experimental data, including those for siderite (Wiesli et al., 2004), goethite (Beard et al., 2010; Frierdich et al., 2014a) and hematite (Skulan et al., 2002; Welch et al., 2003; Saunier et al., 2011) agree well with previous calculations for both solid phases (Polyakov and Mineev, 2000; Polyakov et al., 2007; Blanchard et al., 2009) and aqueous species (Rustad et al., 2010; Polyakov and Soultanov, 2011). In addition, the calculated fractionation factor for stoichiometric magnetite (Mineev et al., 2007) has also been recently proven correct by the experiments of Frierdich et al. (2014b).

Experimental fractionation factors are currently unavailable for pyrite, marcasite, wüstite, and troilite. Moreover, neither experimental nor calculated data for Fe isotope fractionation between pyrrhotite and aqueous Fe^{2+} are available. Schuessler et al. (2007) suggested that troilite (FeS) could be considered representative for high-temperature pyrrhotite. Troilite differs from high-temperature hexagonal pyrrhotite only by a slight distortion from the ideal NiAs structure. They are all members of the same $Fe_{1-x}S$ ($x = 0$–0.125) group, the different pyrrhotite varieties relying on metal vacancies and their arrangements in the basic NiAs crystal structure (e.g., Wang and Salveson, 2005).

A summary of mineral-fluid fractionation trends with temperature in the range of ore-forming systems (Fig. 2) shows the marked differences between troilite (negative)
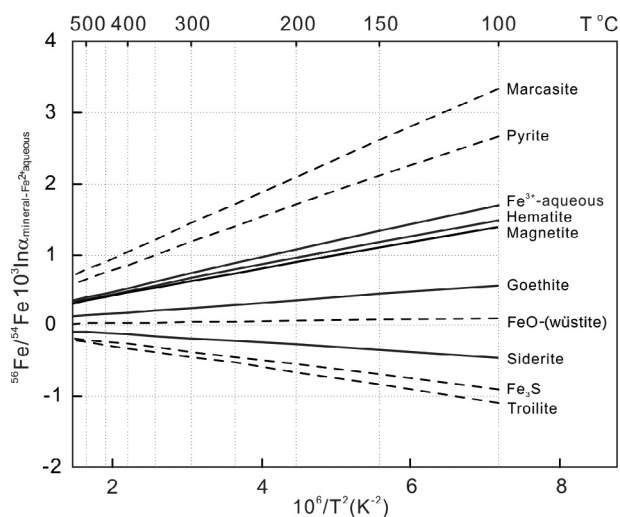

Fig. 2. Temperature dependence of theoretical/experimental δ^{56}-$Fe_{Mineral–Fe(II)}$ for pyrite, marcasite, hematite, Fe(III), magnetite, goethite, FeO-(wüstite), siderite, Fe_3S and troilite. Dashed lines represent theoretical calculations, where the calculated β-factors for marcasite, Fe_3S, troilite and FeO-(wüstite) are from Polyakov et al. (2007); pyrite is from Blanchard et al. (2009); Solid lines represent experimental results. The hematite data is from Saunier et al. (2011); goethite experimental data is from Frierdich et al. (2014a); magnetite from Frierdich et al. (2014b); siderite from Wiesli et al. (2004). Fe(III) data are from Johnson et al. (2002) and Welch et al. (2003).

and pyrite (positive) as a response to temperature, whereas the Fe-oxides/hydroxides show mild variation in Fe-isotope signature relative to wustite (FeO) which nearly remains unchanged with T.

3. GEOLOGICAL SETTING

The giant gold deposits of the Jiaodong Peninsula are located in the southeastern margin of the North China Craton (Fig. 1). These deposits are bounded by the Tan-Lu fault zone to the west, and by the Triassic Dabie-Sulu ultra-high pressure orogenic belt to the southeast. The Sulu orogenic belt resulted from continental collision between the Yangtze Craton and the North China Craton in the Triassic (Li, 1994; Jahn et al., 1996; Zheng, 2008). The ancient Pacific Plate began to subduct beneath Eurasian continent during the Jurassic (Maruyama et al., 1997; Zhou and Li, 2000).

Mesozoic magmatic rocks and Precambrian metamorphosed rock sequences are widespread in the Jiaodong region (Zhou and Li, 2000). Extensive magmatism took place during the late Mesozoic, including emplacement of a series of granitoids and mafic dikes. The granitoids can be divided into two major suites: the Linglong granite (~160 Ma; Ma et al., 2013) and the Guojialing granodiorite (~130 Ma; Hou et al., 2007). Younger mafic dikes (~120 Ma; Ma et al., 2014), including lamprophyres and dolerite-porphyries, intruded both the Linglong and Guojialing granitoid suites and the Precambrian basement. The basement of the Jiaobei terrane is mainly composed of the Neoarchaean Jiaodong Group, including tonalite-throndhjemite-granodiorite (TTG) gneiss, amphibolite and mafic granulite (Jahn et al., 1996; Zhang et al., 2003; Tang et al., 2007).

Two main types of gold deposits are recognized in the district: Linglong type (L-type); and Jiaojia type (J-type). L-type deposits are characterized by auriferous quartz veins, whereas J-type mineralization contains disseminated and stockwork ores within pyrite-sericite and phyllic alteration zones (Lü and Kong, 1993; Qiu et al., 2002; Yang et al., 2014). The majority of both types of gold deposits are hosted within Mesozoic Linglong granite close to fault zones (Fig. 1). L-type deposits occur in small, open fracture systems, whereas J-type deposits are hosted in relatively closed regional ductile-shear fracture systems. Most of the gold deposits comprise a paragenetic sequence of quartz-K-feldspar, quartz-pyrite, quartz-base metal sulfide, and quartz-carbonate (Chen et al., 1989; Lü and Kong, 1993; Zhai et al., 2001; Qiu et al., 2002). L-type deposits are generally rich in sulfides, especially pyrite, in the quartz vein with wall rock alteration haloes dominated by K-feldspar, and less commonly by pyrite–sericite–quartz alteration haloes. In contrast, J-type deposits are characterized by disseminated sulfides in the center of a pyrite–sericite–quartz alteration zone surrounded by haloes of K-feldspar alteration (Fig. 3). Note that the same Linglong granite is the wall rock for both kinds of deposits. Direct Rb-Sr dating of pyrite from the major gold deposits in the Jiaodong district shows gold mineralization occurred at ~120 Ma (Yang and Zhou, 2001; Hou et al., 2006). There is no age
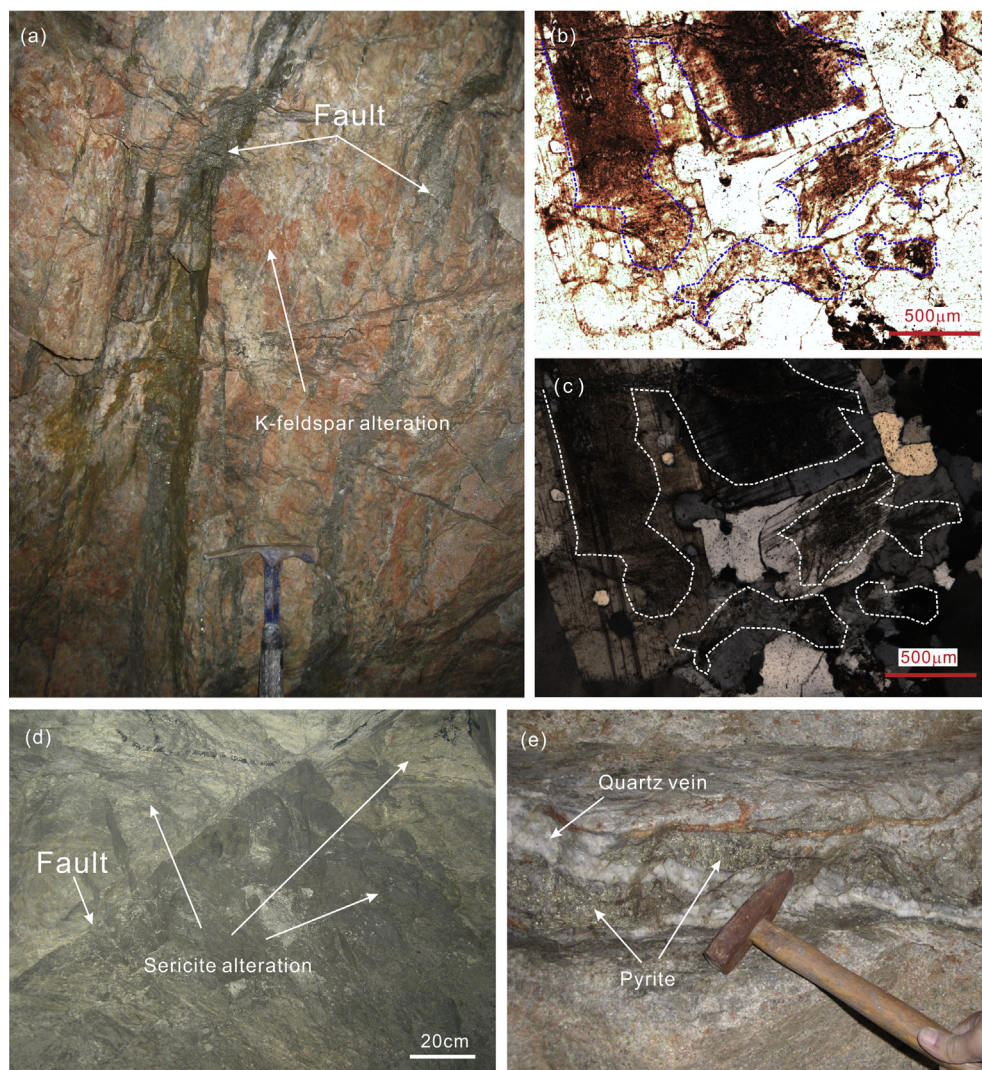
Fig. 3. (a) Typical wall rock alteration for both kinds of gold deposits, pinkish K-feldspar alteration zone of Linglong granite in the gold deposit, (b) and (c) are plane-polarized and crossed polars transmitted light photomicrographs, respectively, of the altered Linglong granite which are characterized by replacement of plagioclase by K-feldspar (dashed line area), (d) sericite alteration zone, where J-type gold deposits are hosted (disseminated pyrite), (e) pyrite-quartz vein, where L-type gold deposits are hosted. Note that faults are developed in the K-feldspar alteration halo, sericite alteration zone and quartz vein (dashed line).

difference between the L- and J-type gold deposits. Both types of deposits belong to the same metallogenic system and formed nearly at the same time, although the mode of occurrence and ore textures are different (Zhai et al., 2001; Zhang et al., 2003; Hou et al., 2006).

4. SAMPLES AND ANALYTICAL METHODS

Samples for this study were collected from drillcores and from underground adits at the Jiaojia, Daliuxing, Heilang-gou, Hexi, Lingnan, Linglong Xishan and Linglong Dong-shan deposits (Fig. 1). Pyrite grains from the gold deposits were hand-picked under a binocular microscope. Basement rocks and K-feldspar altered Linglong granite were col-lected at distances of several to tens of meters outside the

ore body. Fresh Linglong granite was collected from the underground shaft (∼630m) of the Linglong deposit. Whole rock samples of the Linglong granite and Precambrian basement rocks were ground into ∼200 mesh powders.

Whole-rock major and trace element abundances were determined at the State Key Laboratory for Mineral Deposits Research, Nanjing University. Major elements were analyzed by ICP-AES after alkaline fusion digestion, with analytical uncertainties better than 0.5% for all major elements. Trace elements were analyzed on a Finnigan Ele-ment II ICP-MS. About 50 mg of powdered sample was dissolved in high-pressure Teflon bombs using a HF + HNO$_3$ mixture. Rhodium metal was used as an internal standard to monitor signal drift during ICP-MS measure-ment. Two rock standards (GSR-1 and AGV-2) were

Table 1
Analytical results of sulfur and iron isotopic compositions of pyrite samples and iron isotopes of fresh Linglong granite from the Jiaodong gold district.

Sample name	Mineralization type	Sample location	$\delta^{34}S_{V-CDT}$‰	Data source	$\delta^{56}Fe_{-IRMM14}$‰	2SD	$\delta^{57}Fe_{-IRMM14}$‰	2SD	$\delta^{56}Fe_{-sili}$‰
DL-8-4	L type - pyrite	Penglai gold district-Daliuxing	6.4	Hou, 2006	0.76	0.05	1.11	0.10	0.67
DL-8-4[a]					0.75	0.05	1.08	0.10	0.66
HLH-3	L type - pyrite	Penglai gold district-Heilangou	6.3		0.61	0.14	0.94	0.24	0.52
HLH-3[a]					0.61	0.14	1.09	0.24	0.52
DL-9-1	L type - pyrite	Penglai gold district-Daliuxing	6.8		0.46	0.07	0.67	0.10	0.37
DL-9-1[a]					0.45	0.07	0.66	0.10	0.36
HX-11	L type - pyrite	Penglai gold district-Hexi	7.6		−0.35	0.05	−0.40	0.09	−0.44
HX-11[a]					−0.41	0.05	−0.43	0.09	−0.50
HX-12	L type - pyrite	Jiaojia gold districtt-Hexi	7.4		0.66	0.07	1.02	0.14	0.57
HX-13	L type - pyrite	Jiaojia gold districtt-Hexi	7.5		0.64	0.05	0.99	0.09	0.55
HX-14	L type - pyrite	Jiaojia gold districtt-Hexi	8.0		−0.20	0.05	−0.32	0.10	−0.29
HX-15	L type - pyrite	Jiaojia gold districtt-Hexi	8.5		−0.13	0.05	−0.19	0.09	−0.22
LL-171-2	L type - pyrite	Linglong gold district-Lingnan	7.8		0.39	0.05	0.59	0.10	0.30
LL-171-3	L type - pyrite	Linglong gold district-Lingnan	7.0		−0.68	0.05	−1.01	0.10	−0.77
LL-171-6	L type - pyrite	Linglong gold district-Lingnan	8.3		0.05	0.07	0.05	0.10	−0.04
LL-171-7	L type - pyrite	Linglong gold district-Lingnan	7.8		0.46	0.05	0.68	0.12	0.37
LL-171-10	L type - pyrite	Linglong gold district-Lingnan	7.9		0.83	0.05	1.22	0.10	0.74
LL-108-1	L type - pyrite	Linglong gold district-Xishan	7.7		0.10	0.05	0.14	0.10	0.01
LL-108-2	L type - pyrite	Linglong gold district-Xishan	8.3		−0.18	0.05	−0.27	0.10	−0.27
LL-108-5	L type - pyrite	Linglong gold district-Xishan	7.6		−0.08	0.05	−0.13	0.09	−0.17
LL-108-6	L type - pyrite	Linglong gold district-Xishan	8.5		−0.67	0.07	−0.97	0.12	−0.76
LL-108-7	L type - pyrite	Linglong gold district-Xishan	7.5		−0.13	0.07	−0.18	0.10	−0.22
LL-53-4	L type - pyrite	Linglong gold district-Dongshan	7.0		0.37	0.05	0.54	0.12	0.28
LL-48-1	L type - pyrite	Linglong gold district-Dongshan	8.6		0.61	0.05	0.93	0.10	0.52
LL-48-4	L type - pyrite	Linglong gold district-Dongshan	7.2		0.70	0.07	1.05	0.10	0.61
LL-50-3	L type - pyrite	Linglong gold district-Dongshan	6.4		0.77	0.05	1.13	0.09	0.68
LL-50-5	L type - pyrite	Linglong gold district-Dongshan	7.3		0.89	0.05	1.29	0.10	0.80
LL-47-1	L type - pyrite	Linglong gold district-Dongshan	7.4		0.71	0.05	1.10	0.10	0.62
08JJ-05	J type - pyrite	Jiaojia gold district	11.2	This study	0.62	0.09	0.92	0.16	0.53
08JJ-06	J type - pyrite	Jiaojia gold district	11.3		0.67	0.07	0.98	0.14	0.58
08JJ-09	J type - pyrite	Jiaojia gold district	10.3		0.72	0.09	1.07	0.16	0.63
08JJ-11	J type - pyrite	Jiaojia gold district	10.8		0.64	0.09	0.92	0.16	0.55
08JJ-11[a]					0.66	0.09	0.99	0.17	0.57
08JJ-13	J type - pyrite	Jiaojia gold district	11.9		0.61	0.09	0.91	0.14	0.52
08JJ-16	J type - pyrite	Jiaojia gold district	11.6		0.24	0.09	0.29	0.12	0.15
08JJ-18	J type - pyrite	Jiaojia gold district	10.2		0.65	0.09	0.93	0.14	0.56
08JJ-18[a]					0.62	0.09	1.00	0.14	0.53
08JJ-23	J type - pyrite	Jiaojia gold district	9.7		0.59	0.07	0.85	0.14	0.50
08JJ-27	J type - pyrite	Jiaojia gold district	9.8		0.71	0.09	1.05	0.14	0.62
08JJ-30	J type - pyrite	Jiaojia gold district	9.9		0.51	0.09	0.75	0.17	0.42
08JJ-32	J type - pyrite	Jiaojia gold district	9.4		0.62	0.09	0.89	0.16	0.53

(*continued on next page*)

Table 1 (*continued*)

Sample name	Mineralization type	Sample location	$\delta^{34}S_{V\text{-}CDT}$‰	Data source	$\delta^{56}Fe_{\text{-}IRMM14}$‰	2SD	$\delta^{57}Fe_{\text{-}IRMM14}$‰	2SD	$\delta^{56}Fe_{\text{-}sili}$‰
08JJ-35	J type - pyrite	Jiaojia gold district	11.0		0.48	0.07	0.67	0.14	0.39
08JJ-36	J type - pyrite	Jiaojia gold district	10.3		0.58	0.10	0.84	0.17	0.49
08JJ-38	J type - pyrite	Jiaojia gold district	11.1		0.31	0.09	0.48	0.14	0.22
08JJ-40	J type - pyrite	Jiaojia gold district	11.6		0.64	0.07	0.91	0.14	0.55
08JJ-41	J type - pyrite	Jiaojia gold district	10.7		0.63	0.07	0.90	0.14	0.54
08JJ-44	J type - pyrite	Jiaojia gold district	10.9		0.10	0.07	0.21	0.12	0.01
08JJ-47	J type - pyrite	Jiaojia gold district	11.8		0.69	0.07	0.98	0.12	0.60
08JJ-51	J type - pyrite	Jiaojia gold district	10.9		0.71	0.07	1.03	0.14	0.62
08JJ-59	J type - pyrite	Jiaojia gold district	10.2		0.73	0.09	1.07	0.17	0.64
08JJ-59[a]					0.67	0.09	1.00	0.17	0.58
08JJ-75	J type - pyrite	Jiaojia gold district	10.8		0.62	0.09	0.91	0.16	0.53
08JJ-85	J type - pyrite	Jiaojia gold district	11.4		0.73	0.07	1.01	0.12	0.64
08JJ-109	J type - pyrite	Jiaojia gold district	11.0		0.52	0.09	0.77	0.14	0.43
08JJ-121	J type - pyrite	Jiaojia gold district	10.1		0.66	0.10	0.95	0.17	0.57
ZK804-10	J type - pyrite	Jiaojia gold district	11.0		0.64	0.07	0.88	0.14	0.55
ZK804-13	J type - pyrite	Jiaojia gold district	11.5		0.62	0.07	0.85	0.12	0.53
ZK713-5	J type - pyrite	Jiaojia gold district	9.1		0.47	0.07	0.63	0.12	0.38
ZK802-2	J type - pyrite	Jiaojia gold district	10.5		0.39	0.09	0.57	0.14	0.30
ZK717-2	J type - pyrite	Jiaojia gold district	8.8		0.57	0.07	0.81	0.14	0.48
ZK706-5	J type - pyrite	Jiaojia gold district	10.3		0.60	0.09	0.86	0.16	0.51
ZK706-6	J type - pyrite	Jiaojia gold district	11.2		0.66	0.10	0.96	0.12	0.57
ZK715-6	J type - pyrite	Jiaojia gold district	9.5		0.39	0.10	0.56	0.14	0.30
ZK712-2	J type - pyrite	Jiaojia gold district	10.6		0.37	0.09	0.52	0.14	0.28
ZK712-6	J type - pyrite	Jiaojia gold district	10.0		0.56	0.07	0.82	0.14	0.47
ZK704-15	J type - pyrite	Jiaojia gold district	9.8		0.43	0.10	0.60	0.19	0.34
ZK704-18	J type - pyrite	Jiaojia gold district	10.4		0.38	0.09	0.57	0.14	0.29
ZK718-3	J type - pyrite	Jiaojia gold district	11.2		0.48	0.09	0.73	0.16	0.39
ZK709-2	J type - pyrite	Jiaojia gold district	11.2		0.62	0.09	0.93	0.14	0.53
ZK709-9	J type - pyrite	Jiaojia gold district	10.2		0.57	0.09	0.89	0.14	0.48
ZK709-12	J type - pyrite	Jiaojia gold district	10.4		0.34	0.09	0.57	0.14	0.25
LL-B03-01	fresh Linglong granite	Linglong gold district	–		0.12	0.04	0.20	0.10	0.03
LL-B03-02	fresh Linglong granite	Linglong gold district	–		0.10	0.02	0.16	0.02	0.01
LL-B03-03	fresh Linglong granite	Linglong gold district	–		0.11	0.02	0.19	0.06	0.02
LL-B03-04	fresh Linglong granite	Linglong gold district	–		0.11	0.02	0.18	0.02	0.02

[a] Duplicate samples.

Table 2
Iron isotope compositions, major (wt%) and trace element (ppm) compositions of Precambrian metamorphic rocks and K-feldspar altered Linglong granites.

Type	K-feldspar alteration granite							Precambrian metamorphic rocks				
Sample	08JJ-92	08JJ-95	08JJ-101[a]	08JJ-105	ZK701-3	ZK704-5	ZK704-21	08JJ-97	ZK701-2	ZK704-1	ZK705-2	ZK705-3
$\delta^{56}Fe_{-IRMM14}$‰	0.17	0.47	0.66	0.38	0.28	0.48	0.32	0.28	0.17	−0.05	0.20	−0.07
2SD	0.05	0.14	0.10	0.03	0.10	0.19	0.10	0.02	0.12	0.10	0.12	0.10
$\delta^{57}Fe_{-IRMM14}$‰	0.25	0.75	0.66	0.58	0.46	0.75	0.49	0.41	0.27	−0.04	0.36	−0.08
2SD	0.07	0.23	0.14	0.07	0.17	0.31	0.12	0.02	0.19	0.10	0.21	0.12
$\delta^{56}Fe_{-Sili}$‰	0.08	0.38	0.57	0.29	0.19	0.39	0.23	0.19	0.08	−0.14	0.11	−0.16
SiO_2	71.89	74.78	73.17	71.95	74.66	75.61	73.72	45.41	48.42	47.52	64.69	47.23
TiO_2	0.14	0.04	0.08	0.11	0.08	0.03	0.24	2.19	1.37	0.75	0.47	0.93
Al_2O_3	14.61	14.31	10.53	14.16	13.99	13.44	14.56	14.74	11.92	13.16	16.53	15.26
TFe_2O_3	1.16	0.39	5.05	0.65	0.69	0.45	0.58	11.01	15.95	11.73	3.99	12.95
MnO	0.09	0.01	0.03	0.05	0.02	0.04	0.01	0.19	0.33	0.21	0.06	0.22
MgO	0.18	0.06	0.10	0.13	0.16	0.15	0.11	7.58	7.71	10.05	1.78	7.43
CaO	1.65	1.07	0.75	2.03	1.15	1.29	1.03	8.10	10.88	9.47	3.70	11.42
Na_2O	3.78	3.34	0.57	3.01	3.77	4.28	3.25	3.76	1.85	2.11	4.10	2.05
K_2O	3.74	5.20	6.44	5.30	3.91	3.60	5.06	2.52	0.68	0.83	1.54	0.91
P_2O_5	0.11	0.09	0.10	0.12	0.06	0.05	0.09	0.85	0.21	0.12	0.17	0.18
LOI	2.43	0.68	2.81	2.35	1.24	1.00	1.38	4.11	1.69	4.64	3.01	2.32
∑	99.70	99.95	99.59	99.82	99.67	99.90	99.99	99.66	99.92	99.70	99.72	99.92
Li	3.70	0.09	0.67	0.35	5.48	1.12	0.72	31.50	10.50	17.68	19.48	7.38
Be	1.03	1.14	0.48	0.68	0.96	1.19	0.41	1.53	0.99	0.43	0.97	0.50
Sc	0.36	0.61	0.13	0.08	0.41	3.29	297	19.96	34.54	34.67	6.88	44.06
Ti	766	233	521	705	478	185	1432	12485	8218	4342	2981	5991
V	7.68	3.66	5.35	2.72	2.53	1.79	5.77	169	325	225	62.55	280
Cr	4.46	1.46	3.36	4.15	1.73	2.22	5.20	111	241	495	14.62	134
Mn	627	56.6	206	372	129	192	97.5	1306	2612	1435	415	1771
Co	0.57	0.28	3.16	0.50	0.43	0.26	0.76	36.10	45.91	51.31	8.60	44.40
Ni	2.43	1.21	3.78	2.99	1.36	1.85	6.63	113	88.3	167	12.10	50.82
Cu	22.25	3.87	10.50	5.41	2.52	2.11	13.65	39.03	129	25.96	14.32	19.21
Zn	245	311	421	280	139	4.73	894	148	231	110	56.55	122
Ga	10.85	6.21	7.35	13.17	15.66	16.91	12.82	24.13	21.86	16.11	18.56	19.73
Rb	77.4	92.9	139	113	86.4	107	92.4	72.64	12.47	26.86	7.09	26.55
Sr	296	466	179	350	423	49.7	352	2605	221	195	167	153
Y	8.14	2.92	4.98	4.00	6.78	17.75	18.16	30.18	32.10	15.43	10.46	21.82
Zr	84.7	60.0	78.4	113	91.4	73.2	92.7	275	96.4	54.1	178	70.7
Nb	6.52	2.76	5.49	3.98	6.10	13.80	15.50	110	12.0	3.29	13.03	9.42
Mo	0.47	0.32	2.67	1.11	0.72	0.73	0.76	6.59	0.74	0.54	0.41	0.93
Cd	0.00	0.00	4.55	0.06	0.06	0.01	0.02	0.27	0.35	0.23	0.24	0.25
Sn	0.80	0.49	0.51	0.52	1.03	1.63	1.05	2.37	2.69	0.64	1.06	1.08
Cs	0.60	0.57	0.37	0.32	0.84	0.38	0.49	9.49	0.42	1.17	0.73	0.54
Ba	1499	1767	1677	2172	1518	22.83	2744	959	82.1	199	583	156
La	11.16	1.96	5.27	25.61	13.17	3.01	21.36	60.14	10.51	3.58	17.53	9.57
Ce	19.06	5.54	9.71	47.19	23.63	5.30	35.91	106.2	40.11	11.90	42.78	30.99
Pr	2.42	0.40	1.06	4.83	2.75	0.67	4.72	11.78	4.31	1.27	3.60	3.17
Nd	8.97	1.69	3.71	16.66	9.71	2.59	16.86	44.01	20.86	6.59	14.05	14.38

(continued on next page)

Table 2 (continued)

Type	K-feldspar alteration granite							Precambrian metamorphic rocks				
Sample	08JJ-92	08JJ-95	08JJ-101[a]	08JJ-105	ZK701-3	ZK704-5	ZK704-21	08JJ-97	ZK701-2	ZK704-1	ZK705-2	ZK705-3
Sm	1.61	0.41	0.73	2.79	1.69	0.91	2.98	8.67	4.98	1.81	2.42	2.95
Eu	0.81	0.52	0.60	1.03	0.85	0.15	1.64	2.76	1.34	0.73	0.67	0.88
Gd	1.35	0.38	0.65	1.57	1.44	1.31	2.88	7.92	5.65	2.40	2.23	3.36
Tb	0.22	0.07	0.11	0.15	0.19	0.31	0.48	1.05	0.96	0.45	0.35	0.58
Dy	1.49	0.44	0.74	0.77	1.13	2.22	2.93	5.56	6.46	3.03	2.16	4.04
Ho	0.30	0.09	0.16	0.13	0.22	0.57	0.60	1.06	1.20	0.60	0.37	0.79
Er	0.90	0.31	0.45	0.33	0.63	1.74	1.90	2.76	3.68	1.70	1.11	2.33
Tm	0.16	0.06	0.08	0.05	0.09	0.31	0.39	0.38	0.58	0.26	0.16	0.34
Yb	1.16	0.38	0.51	0.34	0.60	2.21	2.49	2.53	3.25	1.43	0.98	2.20
Lu	0.14	0.04	0.07	0.05	0.08	0.37	0.44	0.34	0.48	0.22	0.14	0.34
Hf	2.54	2.74	2.43	2.96	2.97	3.77	2.84	5.66	2.71	1.55	4.17	1.85
Ta	0.42	0.38	0.23	0.14	0.48	1.15	1.59	5.43	0.35	0.12	0.38	0.27
W	1.40	0.20	4.31	0.81	3.03	0.56	2.07	1.26	2.15	0.92	3.28	46.53
Pb	29.99	11.99	1236	78.7	33.42	57.7	14.81	5.62	5.48	3.80	3.80	2.58
Bi	0.15	0.02	10.87	0.19	0.13	0.04	0.18	0.02	1.14	0.15	0.03	0.11
Th	2.75	0.60	3.12	5.42	4.53	7.73	4.14	9.70	0.43	0.20	1.31	0.61
U	0.53	1.25	0.78	0.50	1.26	5.63	0.64	2.11	0.45	0.10	0.24	0.19

[a] This sample may contain some pyrite grains, the TFe_2O_3 and Fe isotope values are highly abnormal; this sample was excluded from further plotting or discussions.

chosen to calibrate element concentrations. Analytical uncertainties were <10%. Analytical procedures for trace elements follow Gao et al. (2003).

Sulfur isotopic compositions of pyrite were measured in the Isotope Geology Laboratory of Institute of Mineral Resources, Chinese Academy of Geological Sciences, using a Finnigan MAT251 mass spectrometer. The method used for sulfur isotopic analysis is similar to Robinson and Kusakabe (1975), in which sulfides are converted to SO_2. The analytical uncertainty is ±0.2‰ for sulfur isotopes.

Measurement of all samples for Fe isotopes was performed at the State Key Laboratory for Mineral Deposits Research, Nanjing University, except for the four fresh granite samples which were analyzed at Createch Testing Technology, Beijing. For Fe isotope analyses, about 10 mg of pyrite samples were digested with aqua regia at 80 °C, and 100 mg of whole rock samples were digested with 2:1:1 $HF:HNO_3:HCl$ at 120 °C for 24 h. After digestion, the samples were evaporated to dryness. Then 1mL HNO_3 was added into each of the beakers to ensure oxidation to Fe^{3+}. After evaporation to dryness, we added 1mL of 10N HCl and closed them, leaving them on a hotplate for a few hours before evaporation to dryness. This step was repeated twice. The further purification follows a revised chromatographic procedure (Zhu et al., 2015) after Maréchal et al. (1999), with which nearly 100% of Fe was collected (see Appendix A). Finally, the separated pure Fe fraction was dissolved in 1% HNO_3, and then Fe isotope ratios were measured using a double focus MC-ICP-MS (Neptune *Plus*) with the ^{56}Fe beam intensity between 13V and 25V. Mass ^{53}Cr and ^{60}Ni were also measured, in order to monitor possible isobaric interferences of ^{54}Cr and ^{58}Ni on Fe measurements. All collectors used in our MC-ICP-MS are faraday cups with the same amplification of 10^{11} Ω. In all cases ^{53}Cr signals were less than 1×10^{-4} V, and no ^{54}Cr correction was needed. Because the polyatomic ions $^{40}Ar^{14}N^+$, $^{40}Ar^{14}N^+$ and $^{40}Ar^{16}OH^+$ represent interferences with the isobaric isotopes $^{54}Fe^+$, $^{56}Fe^+$ and $^{57}Fe^+$, respectively, the MC-ICP-MS was run at a medium resolution mode, enabling resolution larger than 7000. In this mode, the resolving power on the collectors is sufficient to completely separate all polyatomic mass interferences to produce flat top peak sections that are necessary for Fe isotope measurement. Instrument mass bias is generally much larger than natural fractionations, here, our mass bias correction was done by a sample standard bracketing method. The difference of ^{56}Fe intensity between samples and standard was strictly maintained below 10%. The stable introduction system (Finnigan tandem quartz glass spray chamber) was used for sample introduction.

Data were acquired in 3 blocks of analysis and 10 ratios for each block with an integration time of 4.194 s. Measurements are reported as δ ($^{56}Fe/^{54}Fe$) (henceforth $\delta^{56}Fe$) in‰. The δ ($^{57}Fe/^{54}Fe$) (henceforth $\delta^{57}Fe$) was also measured for quality control (Table 1) and to monitor for mass-independent analytical artifacts. Neither artificial nor natural mass independent effects were observed. In Tables 1 and 2, 2 standard deviation is calculated from the instrumental standard error of the $^{56}Fe/^{54}Fe$ or $^{57}Fe/^{54}Fe$ ratios, which represent the total analytical uncertainty
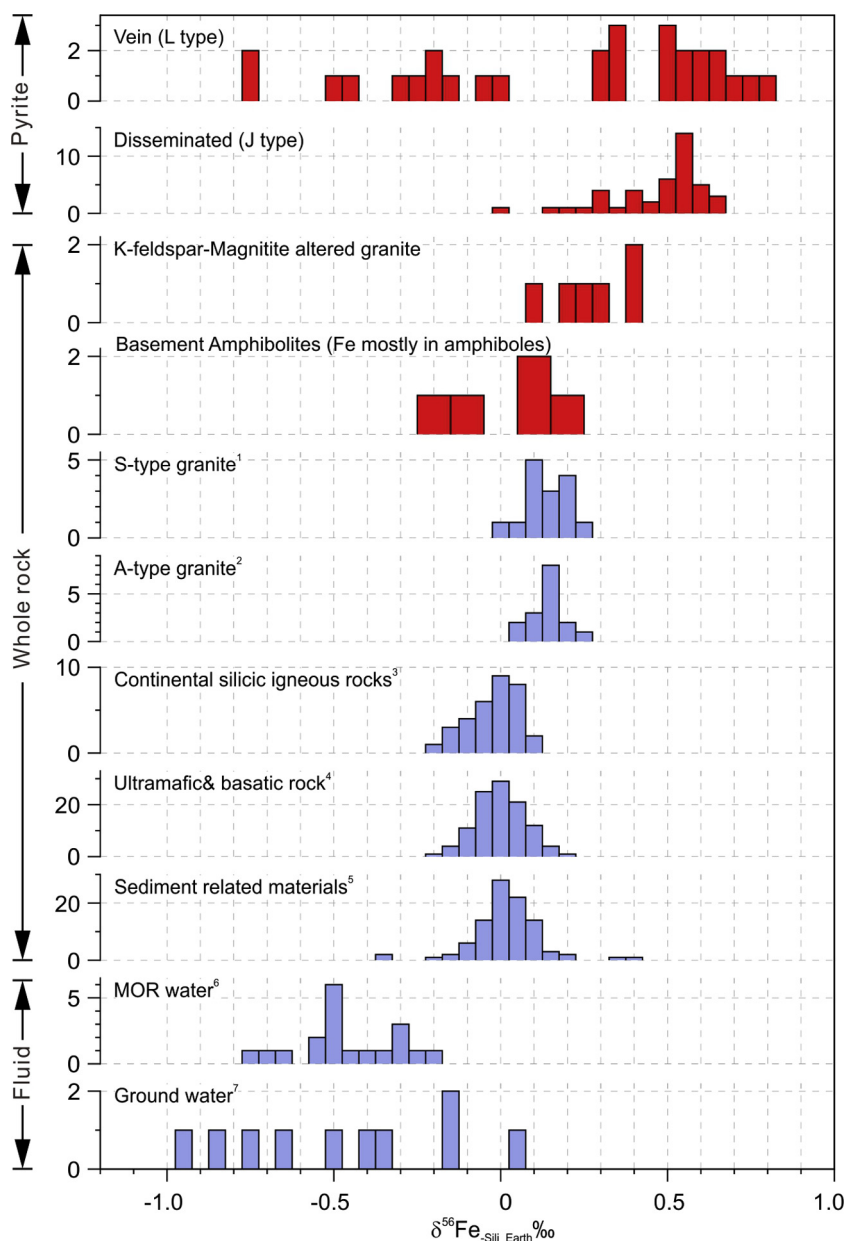
Fig. 4. Histogram of Fe isotope compositions of various reservoirs in comparison with data from the Jiaodong gold province. Data source: 1 Foden et al. (2015); 2 Foden et al. (2015); 3 Beard et al. (2003b) and Foden et al. (2015); 4 Beard et al. (2003b); 5 Zhu et al. (2000) and Beard et al. (2003a) (including soil, clastic/chemically sedimentary rocks, loess and aerosols); 6 Beard et al. (2003a); 7 Fantle and DePaolo (2004) and Bullen et al. (2001). In this figure "zero" means bulk silicate earth Fe baseline. All data have been converted to $\delta^{56}Fe_{sili-earth}$ using the average IRMM-014 value of Beard et al. (2003b) (−0.09‰) Cited $\epsilon^{57}Fe$ data of Zhu et al. (2000, 2001) and $\delta^{57}Fe$ data of Foden et al. (2015) have been transformed to $\delta^{56}Fe$.

including instrumental uncertainties and whole sample processing errors. Each sulfide sample has been analyzed at least 3 times. The silicate rocks have been analyzed at least 4 times. The sample-standard bracketing method was used to calibrate the mass bias of the mass spectrometer with the solution standard IRMM-014. All of the Fe isotope values included in this work have been converted to $\delta^{56}Fe_{silicate-earth}$ using the average IRMM-014 value of −0.09‰ (Beard et al., 2003a). Cited $\epsilon^{57}Fe$ data (Zhu, 2000; Zhu

et al., 2001) and $\delta^{57}Fe$ data (Foden et al., 2015) have also been converted to $\delta^{56}Fe$ to enable a better comparison. These data are normalized to bulk silicate Earth (Beard et al., 2003b), to facilitate tracing the geochemical cycling of Fe. With this definition, the absolute Fe isotope value will be meaningful and can show how anomalous a Fe isotope measurement is relative to a bulk Earth composition. Although the latter study showed that the Fe isotope composition of granitic rocks displays greater scatter than mafic
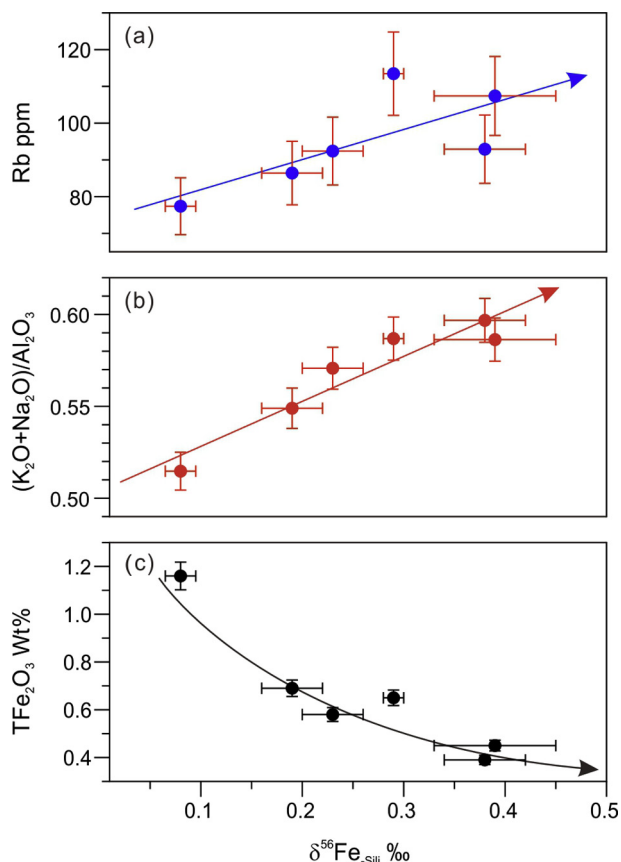
Fig. 5. Diagrams expressing (a) Rb, (b) $(K_2O+Na_2O)/Al_2O_3$ and (c) TFe_2O_3 concentrations vs. Fe isotope value in granite displaying fluid/rock ineraction in K-feldspar alteration zone. With increase in degree of alteration, Rb and $(K_2O + Na_2O)/Al_2O_3$ increase and Fe is continuously leached by the fluid, however, the Fe isotopic composition in the leached granite becomes heavier.

Fig. 6. Histogram plot of S-isotope compositions of the disseminated (J-type) and vein (L-type) pyrite. Data for the L-type are from Ying (1994), Hou et al. (2006) and Mao et al. (2008); data for J-type pyrite are from Mao et al. (2008) and this study. The S isotope composition of J-type pyrite is systematically 3.5‰ heavier than that of L-type.

rocks (Schuessler et al., 2009; Foden et al., 2015), the relatively small amount of crustal granitic rocks would not affect the Fe isotope composition of the large silicate Earth reservoir.

International (BCR-2) and national (GSR-1) rock standard samples were used to check the whole analytical procedure, and a laboratory solution standard (ZXK Fe-115) supplied by Prof. Xiang-Kun Zhu (Chinese Academy of Geological Sciences) was also used to check the mass bias during MC-ICP-MS measurement. Data of all samples in this study were obtained over a period of three days. Six random pyrite samples were re-measured again the following day, and they fall within reported errors. Typical internal precision of the instrument for a single analysis is 0.04‰ (2 standard error, $n = 30$) for $\delta^{56}Fe$. Based on replicate analyses of standards and samples processed through the entire analytical procedure the $\delta^{56}Fe$ values are accurate at 0.06‰ (2 standard deviation) for solution standard, and the accuracy of the solid standard is slightly poorer, at c.a. 0.09‰ (2 standard deviation). Detailed description of our chemical purification procedure and the standard measurement are presented in Appendix A.

5. ANALYTICAL RESULTS

Major and trace elements have been analyzed in five Precambrian metamophic rocks and seven K-feldspar altered Linglong granites. Precambrian metamorphic rocks are amphibolite and granodiorite. The amphibolite smaples show SiO_2 values of 45.5–48.5 wt%, total-Fe_2O_3 (TFe_2O_3) values of 11.0–15.9 wt%, ($Na_2O + K_2O$) values of 2.5–6.2 wt% and Rb concentrations of 12.0–72.6 ppm. Detailed values for a representative granodiorite are given in Table 2. Precambrian metamorphic rocks show $\delta^{56}Fe$ values around 0.0 ± 0.2‰ (Table 2, Fig. 4), i.e., similar to terrestrial rocks.

The SiO_2 contents of K-feldspar altered Linglong granite vary from 71.9 to 75.6 wt%, K_2O ranges between 3.6 and 6.4 wt%, Rb is between 77 and 139 ppm, and TFe_2O_3 is generally <1.2 wt%. The Linglong granite from the K-feldspar alteration halo shows a significantly heavier $\delta^{56}Fe$ character than any published data for terrestrial igneous rocks (+0.08 to +0.39‰; Table 2, Fig. 4). However, the Fe isotope signature of fresh Linglong granite is close to global I-type granite with an average $\delta^{56}Fe_{silicate-earth}$ of 0.02‰ ($n = 4$). Linglong granites are composed of alkali feldspar (30–36 vol%), plagioclase (33–37 vol%), quartz (25–29 vol%), biotite (~5 vol%) and accessory minerals such as magnetite, titanite, apatite, zircon, ilmenite and fluorite. As the wall rock of gold deposit, the granite has experienced widespread K-feldspar alteration around the

orebody, which was characterized by the replacement of plagioclase by K-feldspar. Strong potassic alteration is expressed by secondary K-feldspar in the matrix and within plagioclase phenocrysts, giving the rocks a pinkish appearance (Fig. 3). Iron isotopes show a systematic variation with the degree of alteration (Fig. 5).

Results of Fe and S isotope analyses of pyrites from the Jiaodong gold deposits and the Fe isotope data for fresh Linglong granite are listed in Table 1. The δ^{56}Fe values of the J-type pyrites range from +0.01 to +0.64‰. In contrast, the δ^{56}Fe values of the L-type pyrites show a large range from −0.78 to +0.79‰ (Fig. 4). For comparison, Fe isotopes of typical reservoirs are also plotted in Fig. 4. Pyrites from the J-type deposits show a δ^{34}S variation range between +8.5 and +12.5‰, with a peak value at +11.0‰, while the δ^{34}S values of the L-type pyrites vary from +6.3 to +10.7‰, with a peak value at +7.5‰ (Fig. 6). The sulfur isotopic composition of the J-type pyrites shows a systematically higher value, about +3.5‰ greater than that of the L-type pyrites. No correlation between Fe and S isotope signatures in pyrite has been observed in this study, although the sources of Fe and S in the two deposit types are generally thought to be the same. They may be linked with different fractionation mechanisms and differing controlling factors, as will be discussed below.

5.1. Ranges of Fe isotopes in basement rocks, granites and pyrites

The Precambrian basement of the Jiaobei terrane is mainly composed of the Neoarchaean Jiaodong Group, including TTG gneiss, amphibolite and mafic granulite (Zhang et al., 2003; Tang et al., 2007; Jahn et al., 2008). In our research area, the basement rocks are mainly amphi-

bolites. Analysis of five representative whole rock samples shows that δ^{56}Fe ranges from −0.16 to 0.19‰, similar to bulk silicate Earth (Fig. 4). In general, Fe isotope values of sediment-related materials (e.g., soils, marine/continental sediments, loess/aerosols (Zhu et al., 2000; Beard et al., 2003b), and igneous rocks (e.g., ultramafic, basaltic, continental silicic igneous rocks) cluster around zero (δ^{56}Fe ≈ 0 ± 0.2‰) (Zhu et al., 2000; Beard et al., 2003b). A-type and S-type granites are an exception, having slightly heavier Fe isotope signatures (δ^{56}Fe ≈ 0.15 ± 0.1‰) than I-type granite or other terrestrial igneous rocks, resulting from redox conditions and the assimilation-fractional crystallization process of the magmas (Foden et al., 2015). Unequivocal proof of any Fe isotope variation or heterogeneity within the Neoarchaean Jiaodong Group will require additional analysis of a larger suite of samples, and is beyond the scope of the present study. Despite this, the Precambrian basement of the Jiaobei terrane clearly shows a distinct Fe isotope signature from that of the K-feldspar altered Linglong granite, but similar to bulk silicate Earth.

As shown in Fig. 4, pyrite in L-type deposits displays a large variation of Fe isotope composition. Generally, the heavier Fe isotope tends to be enriched in pyrite relative to solution. Depletion in fluid systems (Fig. 4) has been documented from vent fluids on the Juan de Fuca Ridge setting (Sharma et al., 2001), mid-ocean-ridge setting fluids (Beard et al., 2003a) and in groundwaters (Bullen et al., 2001; Fantle and DePaolo, 2004).

5.2. Ranges of S isotopes in pyrite and their potential source

Sulfur isotopes of vein (L-type) pyrite are positive (~7.5‰), although ~3.5‰ lighter than disseminated (J-type) pyrite (~11.0‰) (Fig. 6). The heavy S isotope signature of both deposit types indicates that the sulfur is derived from the reduction of sulfate. For orogenic Au deposits hosted by sedimentary rocks, S isotope compositions generally show a pattern that parallels the seawater sulfate curve through geologic time, indicating that the sulfur in most sediment-hosted orogenic Au deposits probably originated from the reduction of seawater sulfate (Chang et al., 2008). Similar phenomena have been found in VHMS and SEDEX Cu-Zn-Pb deposits (Sangster, 1968; Goodfellow et al., 1993; Huston, 1999), a strong argument favoring the derivation of S in these deposits from reduced seawater sulfate rather than from magmatic or metamorphic sulfur.

In contrast, gold deposits in Jiaodong are hosted in granite, there are no Phanerozoic sedimentary sequences in the region, and the basement rocks are Neoarchaean rocks of the Jiaodong Group (TTG gneiss, amphibolite and mafic granulite; Zhang et al., 2003; Tang et al., 2007; Jahn et al., 2008). Unlike sediment-hosted orogenic gold deposit, VHMS or SEDEX Cu-Pb-Zn deposits, the wall rocks of the Jiaodong gold deposits could not supply seawater sulfate. Another possible source of heavy S is, however, recycled seawater in ore-forming fluids. H-O isotope compositions of the fluid inclusions suggest, however, that the fluids are of magmatic origin (Fan et al., 2003), thus ruling out any role for recycled seawater. Considering that
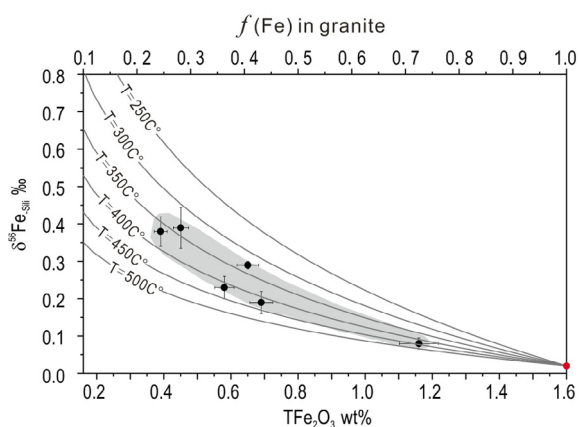

Fig. 7. Modeling of Fe isotope signature vs. Fe concentration in the granite during alteration at various temperatures. The initial Fe isotope composition of the Linglong (I-type) granite is from the fresh granite (0.02‰, n = 4). The initial TFe$_2$O$_3$ wt% of the fresh Linglong granite is defined as 1.6% from Hou et al. (2007). The residual phase of the altered granite was represented by magnetite. The fractionation factor between fluid and magnetite is from the experimental study of Frierdich et al. (2014b). The spots are measured results of the altered granite. It suggests that the alteration temperature is 381 ± 45 °C (2 standard errors).
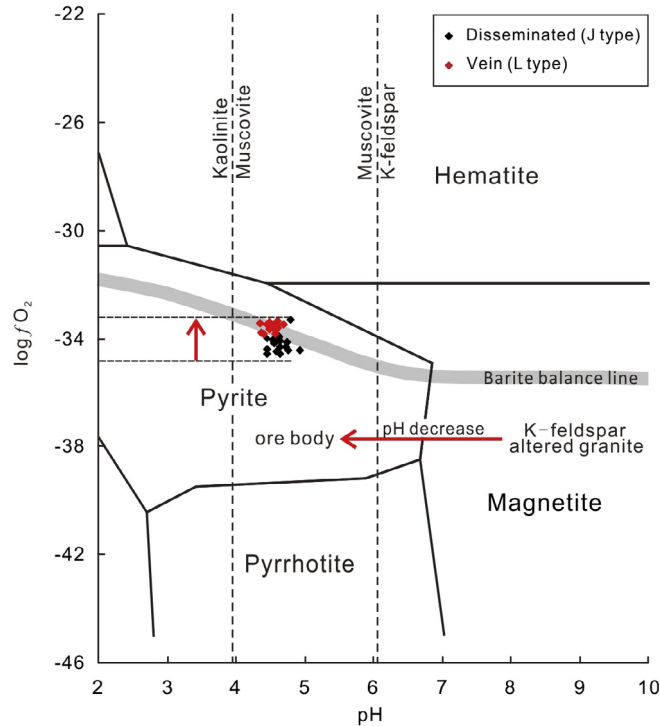
Fig. 8. Influence of f_{O_2} and pH on the iron species ($T = 300$ °C, $\sum$Fe = 1000 ppm, NaCl = 10%, ion activity of Fe^{n+} and $K^+ = 1$, using PHREEQC) and the equilibrium iron isotope compositions of iron species. Solid lines represent the boundaries of Fe-oxide or -sulfide stabilities. The dashed lines show the kaolinite, muscovite and K-feldspar buffer (after Cooke et al., 1996, assuming $\alpha_{K^+} = 0.00437$). The pH decreases from the K-feldspar alteration zone to the ore body. An approximate $BaSO_4$ line is included in this figure. The spots are the physicochemical conditions calculated from the composition of ore-forming fluids in the co-existing gangue minerals. All spots are located in the pyrite field, fully consistent with geological observation. However, vein (L-type) deposit has a slightly higher oxygen fugacity than disseminated (J-type) deposits, which is near the buffer zone of SO_4^{2-}, causing the lighter S isotopic signature of vein (L-type) pyrite.

there exist a great many of mafic dikes, which are linked to subduction of the Palaeo-Pacific plate nearly at the same time as mineralization, sedimentary materials derived from the slab are a possible sulfur source.

6. DISCUSSION

Progressive alteration in granite can be modeled using Fe isotope values and whole rock compositions of potassic-altered granite (Table 2, Fig. 4), in which the main Fe-bearing mineral is magnetite, and sulfides are absent. Iron and S isotope fractionation during ore deposition in the two deposit types can be discussed in terms of fluid parameters calculated from published fluid inclusion data. Altogether the data can be placed within a conceptual model based on the two types of gold mineralization studied here they also have potential application to deposits elsewhere.

6.1. Fluid/rock interaction in K-feldspar alteration zone – Fe isotope fractionation and temperature estimates

δ^{56}Fe values for Linglong granite within the K-feldspar alteration halo range from +0.08 to +0.39‰, which is clearly heavier than fresh granite (+0.02‰). The Linglong granite was derived by partial melting of Neoarchaean

metamorphic lower-crustal rocks at a depth of >50 km with an eclogite residue (Hou et al., 2007). Differentiation of ultramafic–mafic magmas results in the heavy Fe isotope being enriched both in late-stage melts and olivine crystals (Teng et al., 2008). Removal of light iron isotopes from the magma by aqueous fluids exsolved during late granite evolution could also result in heavy iron isotope in the granite (Poitrasson and Freydier, 2005). The Fe isotope signature of high-silica igneous rocks may be as high as +0.3‰, and the δ^{56}Fe composition of magnetite within those rocks can even be as high as +0.45‰ (Heimann et al., 2008). Such heavy δ^{56}Fe values may be restricted to the exsolution of chloride-containing fluids in highly-evolved rocks (Heimann et al., 2008), rather than to the fractionation crystallization process itself. Through modeling the evolution processes of A-, I- and S-type granites, Foden et al. (2015) proposed that f_{O_2}, whether the system is open or not, and the AFC process of a magma, control the iron isotope composition of granite. Although the exact cause of the heavy iron isotope enrichment in S- and A-type granite, or in high-silica igneous rocks, remains under debate, the highest δ^{56}Fe previously reported for granite to date is <0.3‰ (Poitrasson and Freydier, 2005; Heimann et al., 2008). Due to the similarity in geochemical characteristics between K and Rb, Rb can be incorporated in K minerals. Rocks that have undergone potassic alteration display a

two- to threefold increase in Rb and high Rb/K ratios (Armbrust et al., 1977). In the present study, the Rb concentration is a good indicator of the degree of K-feldspar alteration in Linglong granite. As shown in Fig. 5, as alteration increases, Rb concentrations increase, TFe$_2$O$_3$ decreases and the δ^{56}Fe values correspondingly increase. Continued pervasive leaching may allow the granite to be one source of iron, however, the granite could not supply such a huge amount of Fe for the deposits (which contain an estimated >10 Mt pyrite). The basement rock is another possible source of Fe. TFe$_2$O$_3$ of the basement rock in Jiaodong exceeds 10 wt%. The Fe isotope signature of the basement rock is, however, hard to modify via fluid-rock interaction, unlike the granite. The basement rock thus shows a similar Fe isotope composition as the bulk silicate Earth.

Assuming no Fe isotope exchange happens between solid and hydrothermal fluid, the only function of the fluid is to remove Fe from the granite, and there should be no correlation between TFe$_2$O$_3$ wt% and δ^{56}Fe. However, analytical data show a clear negative trend between TFe$_2$O$_3$ wt% and δ^{56}Fe, inferring that the fluid not only removed Fe from the granite but also exchanged with the granite, preferentially removing the lighter Fe isotope. Hence, we chose the Rayleigh fractionation model. Linglong granite is a weakly peraluminous I-type granite (Ma et al., 2013).

δ^{56}Fe of I-type granite is generally clustered around 0.00‰ (Foden et al., 2015), Linglong granite is no exception (δ^{56}Fe = 0.02‰, n = 4) (Table 1). The average TFe$_2$O$_3$ concentration of fresh Linglong granite is 1.6 wt% (Hou et al., 2007). The initial system is thus defined to have a δ^{56}Fe value of 0.02‰ with 1.6 wt% TFe$_2$O$_3$.

The two main host minerals for Fe in I-type granite are magnetite and biotite. Due to the absence of a Fe isotope fractionation factor for biotite, and biotite in any case accounting for <5% of the total minerals, magnetite was used as the residual solid phase. The fluid (Fe$^{2+}_{aq}$) and magnetite fractionation factors are from the experimental study of Frierdich et al. (2014b): $10^3 \ln\alpha$Fe$^{2+}_{aq}$–magnetite = −0.145 ($\pm$0.002) × 10^6/T^2 + 0.10 ($\pm$0.02).

$$\delta^{56}Fe_{-altered\ granite} = \left(f^{\alpha-1} - 1\right) \times 1000‰$$

where f represents the proportion of Fe left in the granite, α is the fractionation factor between fluid and magnetite, and δ^{56}Fe$_{-altered\ granite}$ is the Fe isotope composition of altered granite. Modeling results are shown in Fig. 7.

Based on the data here, the calculated temperature of K-feldspar alteration in the Linglong granite is between 300 °C and 400 °C (mean 381 $\pm$ 45 °C; Fig. 7). Such a temperature range is slightly higher than the estimated temperature of ore formation (200–350 °C; Xu et al., 1996; Lu et al., 1999; Shen et al., 2000; Fan et al., 2003;
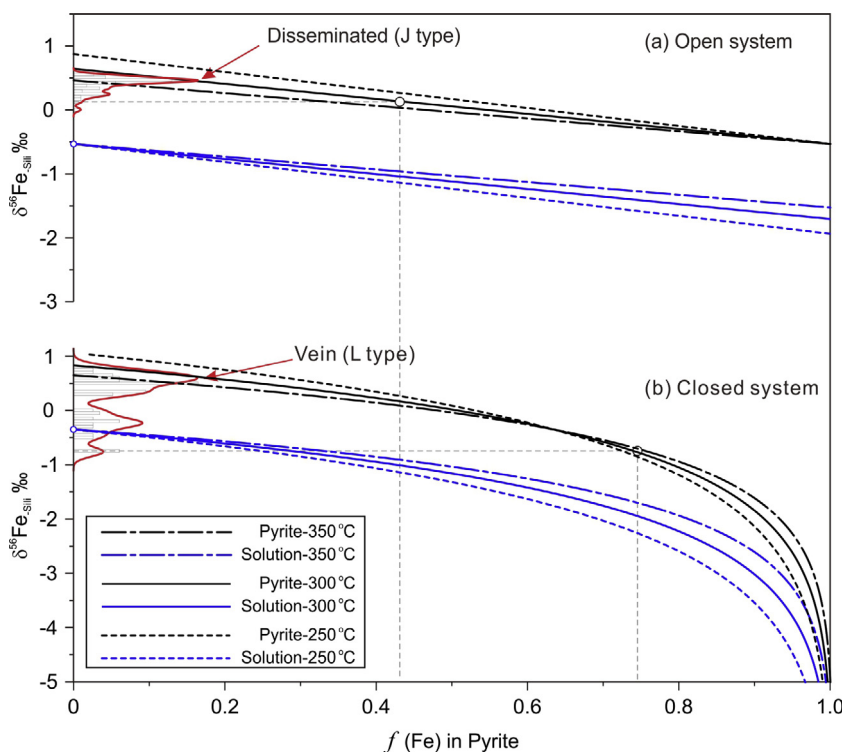

Fig. 9. Model fractionation of Fe isotopes in closed and open systems for the pyrite-solution system at various temperatures. Notice that the open or closed system is for elemental Fe. The fractionation factor between pyrite and solution is given by Blanchard et al. (2009). The initial Fe isotope values are defined as −0.53‰ and −0.37‰ for J- and L-type fluids, respectively, according to their maximum Fe isotope value at 300 °C. A histogram of Fe isotope compositions in the two deposit types is also plotted along the vertical axis. The variation of Fe isotope values is relatively small in the open system, however, the Fe isotope composition in the closed system could be even lighter than that of the initial fluids.
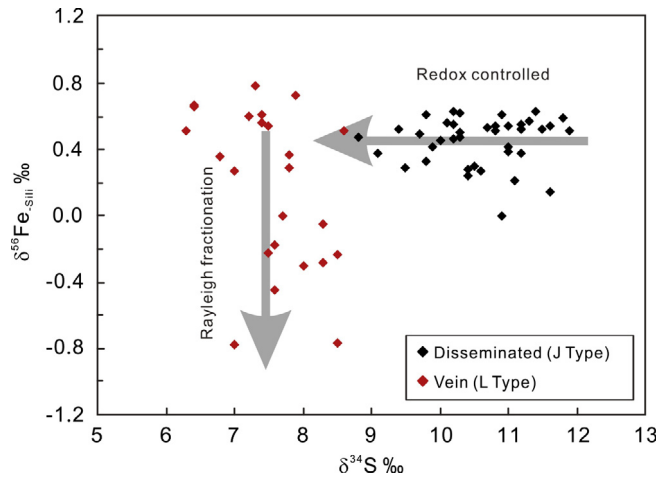
Fig. 10. Co-variation of $\delta^{56}Fe_{-silicate\ earth}$ vs. $\delta^{34}S$ for vein (L-type) and disseminated (J-type) pyrite. The S isotope variation between these two deposits is controlled by redox conditions of the ore-forming fluids, whereas the large variation of Fe isotope compositions in the disseminated deposits is caused by Rayleigh fractionation. Hence, Fe and S isotopes are interpreted to be decoupled.
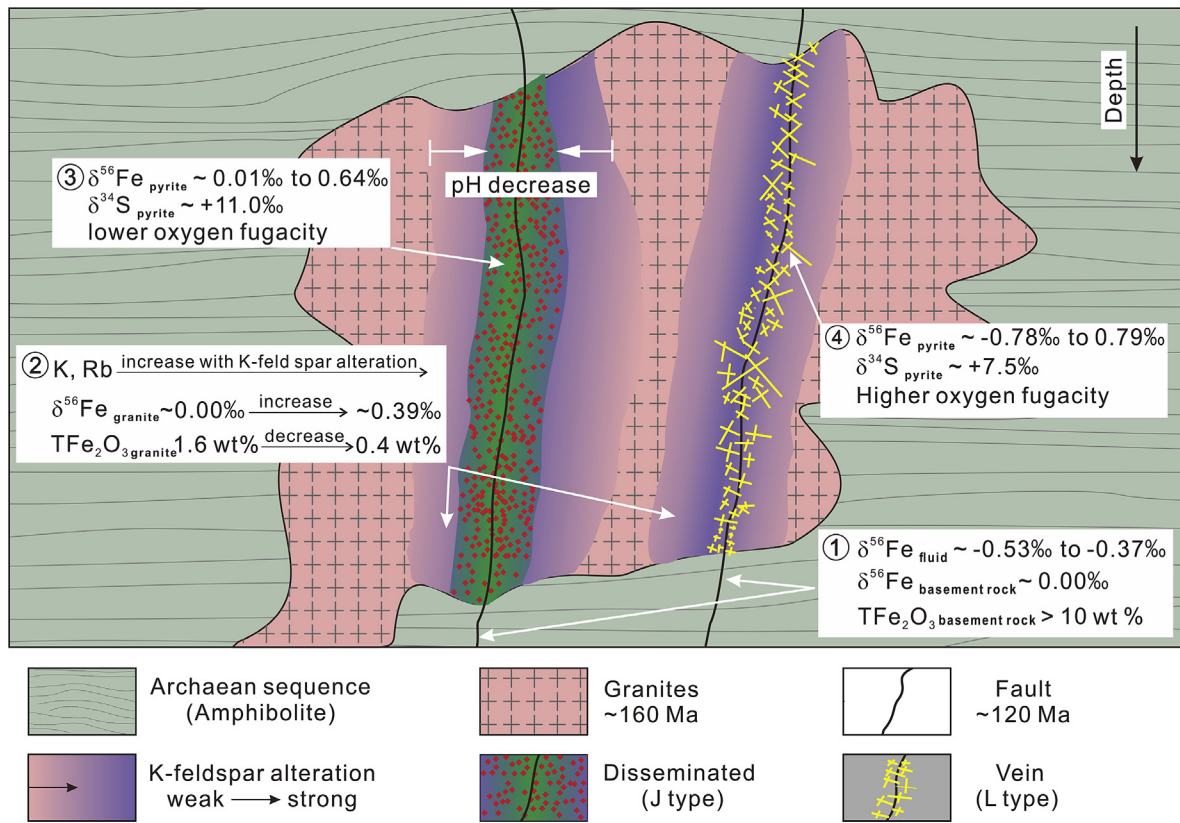

Fig. 11. Schematic cross-section showing the two kinds of gold deposits within a simplified ore-forming system.

Yang et al., 2009), based on studies of fluid inclusions in quartz from the orebodies (including sericite alteration zone and quartz veins). Therefore, the ~50 °C temperature difference suggests that K-feldspar alteration of granite could have provided a minor source for the Fe, since hydrothermal magnetite associated with K-feldspar formation interacts with the hydrothermal fluid to form pyrite during gold deposition.

6.2. Ore deposition – Fe and S isotopes in pyrite

Both iron and sulfur are redox sensitive elements, and fractionation of these isotopic systems may relate to the variation in redox condition of the hydrothermal fluids from which they precipitated. For better discussion and modeling, a mineralizing temperature of 300 °C is used for the precipitation of pyrite from hydrothermal solution

for both deposit types, and calculation shows that a variation of temperature of <100 °C will not cause any significant effects on the modeling results of the Eh or pH evaluation. Fluid inclusion studies have shown that these deposits were formed from CO_2-bearing fluids with generally minor concentrations of CH_4. For example, the molar fraction of CH_4 (X_{CH4}) in fluid inclusions in the CO_2-CH_4-H_2O system at the Sanshandao gold deposit (J-type) is 0.05–0.15 with an average of 0.08 (Fan et al., 2003). In the Dayingezhuang gold deposit (J-type), X_{CH4} is 0.002–0.05 with an average of 0.02 (Yang et al., 2009), and in the Linglong gold deposit (L-type) X_{CH4} is 0.0001–0.002 with an average of 0.0006 (Xu et al., 1996). Hence, the fluid inclusions of the J-type contain more CH_4 compared with the L-type. Correspondingly, the calculated $\log(f_{O2})$ of the J-type fluids is −34.6 to −33.9, whereas it is −33.9 to −33.3 for L-type fluids, using the calculation method of Liu and Shen (1999). According to Crerar et al. (1978), the pH of a CO_2-H_2O-NaCl system could be evaluated with CO_2 pressure and NaCl salinity. The pH of both the J- and L-type ore-forming fluids has been calculated from the fluid inclusion composition data given by Xu et al. (1996) and Yang et al. (2009). Evaluated pH values of the two deposit types are similar (pH = 4.3–4.9). The pH and $\log(f_{O2})$ of both types of fluid inclusions are plotted in Fig. 8. Both J- and L-type fluid inclusions are located in the pyrite box on the figure, although the $\log(f_{O2})$ for the L-type is larger than that of the J-type. Note also that the data plot within the sericite stability field relative to K-feldspar. The boundary between the sericite and K-feldspar also constrains pH to have decreased from potassic altered granite to pyrite deposition; such variation may also impact on isotopic fractionation.

Although there is a modest difference in redox condition between the two types of pyrite, the absence of co-existing hematite/magnetite with pyrite in both ore types places constraints on the relative f_{O2} and pH of the hydrothermal fluids (Fig. 8). Previous studies (Anbar et al., 2005; Polyakov et al., 2007) have shown that heavy iron isotopes tend to be more enriched in pyrite than hematite and Fe^{3+} (aqueous) (Fig. 5). If a large redox variation had been involved during formation of the L-type ores, in order to cause such a large $\delta^{56}Fe$ drift in the L-type pyrites, there must have been a significant amount of either aqueous Fe^{3+}, or hematite/magnetite and/or pyrrhotite present in the ore-forming system. However, this is in contradiction with the observations in the Jiaodong gold deposits. Hence, f_{O2} conditions during formation of the L-type ores were insufficiently high to form any Fe^{3+}-bearing minerals such as hematite or magnetite, even though f_{O2} of L-type ores is higher than that of the J-type (Fig. 8).

Sulfur isotope fractionation between sulfide and hydrothermal fluids is controlled by f_{O2} and pH of the fluids (Ohmoto, 1972). Differences in $\delta^{34}S$ values between the L- and J-type pyrites can be explained using the well-established model given by Ohmoto. As discussed above, L-type quartz vein pyrite formed at higher f_{O2} than the J-type ores, an interpretation concordant with fluid inclusion evidence in the two deposits (Fig. 8). As a result, the amount of SO_4^{2-}, or the SO_4^{2-}/H_2S ratio in fluid responsible

for the L-type deposit is larger than for the J-type, which will cause the $\delta^{34}S$ of precipitated L-type pyrite to be lighter than those of the J-type pyrite.

Therefore, the significant difference in $\delta^{56}Fe$ between vein and disseminated pyrite (L- and J-types, respectively) is unlikely to be caused simply by redox state of Fe in the fluids, even if this may be the underlying reason for the difference in the sulfur isotope signatures of pyrite. Other factors must have induced Fe isotope fractionation. Sulfur and Fe isotopes are considered to display decoupling in this study, although coupled fractionation behavior has been reported elsewhere e.g. microbial reduction process (Archer and Vance, 2006).

6.3. System thermodynamics and a conceptual model for the two deposit types

Before modeling Fe isotope fractionation of the two deposits, it is important to establish whether the Fe isotope signature of the pyrite in this study represents the product of kinetic or equilibrium fractionation. Both experimental studies (Butler et al., 2005) and investigations of natural systems (Gagnevin et al., 2012; Gao et al., 2017) suggest that Fe isotope ratios in pyrite sometimes responds to kinetic fractionation, resulting in a lower Fe isotope value in pyrite than the solution, however, this is only true when the aqueous Fe^{2+} activities are significantly greater than S^{2-}, and the precipitation of mackinawite (an intermediate phase during the formation of pyrite) is fast. In environments with ppm or grater ΣS concentrations ($\geq 10^{-3}$ M), the rate of sulfide formation is two orders of magnitude greater in neutral to alkaline systems than that of acid systems with pH < 7 (Rickard, 1995). High sulfur concentration is typical for environments of sedimentary pyrite formation, hence, kinetic Fe isotope fractionation in pyrite has been reported for some sedimentary related deposits (Gagnevin et al., 2012; Gao et al., 2017). Such a phenomenon is, however, rarely found in high-temperature hydrothermal systems (Wang et al., 2011, 2015; Wawryk and Foden, 2015), especially those where the fluids have low pH (Graham et al., 2004). The calculated pH value of ore-forming fluids in Jiaodong gold deposits ranges from 4.3 to 4.9, in this case, the sulfide precipitation rate is low and kinetic fractionation is unlikely to happen (Rickard, 1995). Furthermore, the S isotope signature of co-existing sulfides ($\delta^{34}S_{pyrite} > \delta^{34}S_{sphalerite} > \delta^{34}S_{chalcopyrite} > \delta^{34}S_{galena}$) has shown that these sulfides are in equilibrium with one another (Wang et al., 2002). Finally, pyrite has the heaviest Fe isotope signature in the whole ore district, so if the Fe isotope signature of pyrite is a function of kinetic fractionation, the Fe isotope composition of the ore-forming fluid should be heavier than any minerals and rocks in the district, which is obviously illogical. Hence, this study adopts equilibrium fractionation as the factor to explain observed patterns.

The Fe isotope data obtained for pyrite in the two deposit types can be also used to assess the type of thermodynamic system in which the two types of ores form (Fig. 9). Fluid (Fe_{aq}^{2+}) and pyrite fractionation factors are taken from the most recent theoretical calculations

(Blanchard et al., 2009), $10^3 \ln\alpha Fe^{2+}_{aq}$–pyrite = 0.8291 × $10^6/T^2$ −3.2161 × $10^9/T^4$ + 1.7889 × $10^{13}/T^6$. The highest $\delta^{56}Fe$ values for J- and L-type pyrite are +0.64‰ and +0.80‰, respectively. The fractionation factor between fluid and pyrite is −1.17‰ at 300 °C (Blanchard et al., 2009). The initial $\delta^{56}Fe$ value is hence set to −0.53‰ for

Table A
Fe isotope measurements of reference standards BCR-2 and GSR-1.

Name	$\delta^{56}Fe_{-IRMM14}$‰	2δ	$\delta^{57}Fe_{-IRMM14}$‰	2δ
BCR-2	0.12	0.04	0.18	0.09
	0.06	0.04	0.07	0.08
	0.16	0.05	0.25	0.08
	0.10	0.05	0.20	0.10
	0.06	0.04	0.10	0.08
	0.18	0.05	0.31	0.08
	0.16	0.05	0.18	0.10
	0.07	0.05	0.06	0.09
	0.09	0.04	0.07	0.09
	0.11	0.05	0.15	0.09
	0.04	0.05	0.11	0.08
	0.16	0.05	0.27	0.08
	0.08	0.04	0.12	0.08
	0.05	0.06	0.09	0.09
	0.13	0.05	0.17	0.08
	0.07	0.05	0.07	0.08
	0.09	0.04	0.10	0.08
	0.09	0.05	0.09	0.08
	0.08	0.04	0.14	0.09
	0.15	0.04	0.25	0.09
	0.07	0.04	0.10	0.09
	0.16	0.05	0.27	0.09
	0.04	0.05	0.11	0.10
	0.05	0.04	0.12	0.09
	0.10	0.05	0.23	0.08
	0.17	0.04	0.17	0.08
	0.07	0.04	0.14	0.08
	0.09	0.04	0.08	0.08
	0.05	0.05	0.12	0.08
Average	0.10		0.15	
SD	0.04		0.07	
2δ	0.02		0.03	
GSR-1	0.22	0.04	0.31	0.08
	0.12	0.04	0.19	0.08
	0.14	0.04	0.19	0.08
	0.21	0.04	0.30	0.08
	0.15	0.04	0.22	0.08
	0.19	0.04	0.29	0.07
	0.18	0.05	0.28	0.08
	0.22	0.04	0.35	0.08
	0.16	0.04	0.28	0.08
	0.18	0.04	0.25	0.08
	0.17	0.05	0.33	0.08
	0.17	0.04	0.26	0.08
	0.16	0.05	0.24	0.08
	0.18	0.05	0.23	0.09
	0.15	0.04	0.18	0.09
	0.14	0.04	0.20	0.09
	0.14	0.05	0.28	0.09
	0.15	0.04	0.19	0.08
	0.21	0.04	0.23	0.08
Average	0.17		0.25	
SD	0.03		0.05	
2δ	0.01		0.02	

J-type, and −0.37‰ for L-type, values very similar to the Fe isotope composition of hydrothermal and groundwater systems (Bullen et al., 2001; Sharma et al., 2001; Beard et al., 2003a; Fantle and DePaolo, 2004). There appears to be a small fractionation between fluids from the two deposit types. Considering the relatively large variation in estimated ore-forming temperature (∼200 to ∼350 °C; Xu et al., 1996; Lu et al., 1999; Shen et al., 2000; Fan et al., 2003; Yang et al., 2009), we assume a value of 300 °C for both types of deposits. There is no significant difference whether the Fe isotope composition of the fluid is set at −0.53‰ or −0.37‰, and no influence on the modeling of fractionation behavior in Fig. 9. For comparison, models at 250 °C and 350 °C are presented in the same figure.

Disseminated (J-type) pyrite occurs in the sericite alteration zone in which Fe is present in wall rock dominantly as magnetite. Iron can thus be exchanged between pyrite and wall rock under high fluid/rock alteration conditions; i.e., the system is open for Fe. In contrast, vein (L-type) pyrite is hosted in quartz veins. After crystallization, pyrite becomes isolated from flow of hydrothermal fluid by quartz, precluding isotopic exchange (closed system). As Fe concentrations in the hydrothermal fluid wane, the Fe isotope signature of vein (L-type) pyrite decreases rapidly, contributing to the large Fe isotope variation in L-type pyrite. Due to the different fractionation mechanism of S and Fe isotopes in this study, Fe and S isotopes show a decoupling behavior (Fig. 10).

Based on the above results a conceptual model can be put forward to explain the variation in isotope fractionation observed in the two types of gold deposits (Fig. 11). This considers four stages:

(1) Hydrothermal fluid infiltrates basement rock and fluid-rock interaction takes place. However, due to the relatively high total Fe in the basement rocks ($TFe_2O_3 > 10\%$), no significant Fe isotope fractionation takes place ($\delta^{56}Fe \approx$ silicate Earth). The Fe isotope composition of the hydrothermal fluid is −0.53‰ to −0.37‰.

(2) The fluid migrates upwards along faults and reacts with I-type Linglong granite ($TFe_2O_3 = 1.6$ wt%), forming a K-feldspar alteration halo. With an increasing degree of alteration, TFe_2O_3 of the granite decreases to 0.39 wt% but the Fe isotope composition increases to 0.39‰.

(3) With a decrease of fluid pH, pyrite starts to precipitate as disseminations within the sericite alteration zone (J-type mineralization). The wall rock contains variable Fe and is effectively an open system with respect to Fe. The variation in the Fe isotope signature is hence relatively narrow (from 0.01‰ to 0.64‰).

(4) Pyrite precipitates within quartz veins (L-type mineralization), representing a relatively closed system with respect to Fe. Late-stage pyrite in this kind of deposit could have an extremely light Fe isotope signature with a large variation (from −0.78‰ to 0.79‰). Note that there is no prioritization for stages (3) and (4), they could form at the same time. Sulfur isotope variation in pyrite from the two deposits responds to changes in the f_{O2} of the ore-forming fluid.

6.4. Comparison with other hydrothermal ore deposits

Several other Fe isotope studies of pyrite from magmatic-hydrothermal ore deposits exist in the literature. Skarn deposits have been the most systematically investigated, including studies addressing co-existing mineral pairs (Graham et al., 2004; Wang et al., 2011; Wawryk and Foden, 2015; Wang et al., 2015; Zhu et al., 2016), Fe isotope fractionation during skarn-type alteration (Zhu et al., 2016), and the temporal/spatial evolution of Fe isotopes (Wang et al., 2011, 2015). Both whole rock (Wang et al., 2015) and separated pyrite grains (Wang et al., 2011) from exoskarn have heavier Fe isotope compositions than endoskarn, a phenomenon believed to be related to fluid exsolution, although the detailed mechanism remains to be investigated (Wang et al., 2011, 2015). Iron isotope variation in skarn has been linked to processes of mineral precipitation from ore-forming fluid (Wang et al., 2015). It was observed that heavy Fe isotope was removed from the protolith by solution during metasomatism (Zhu et al., 2016). The cause of this is unclear at present,
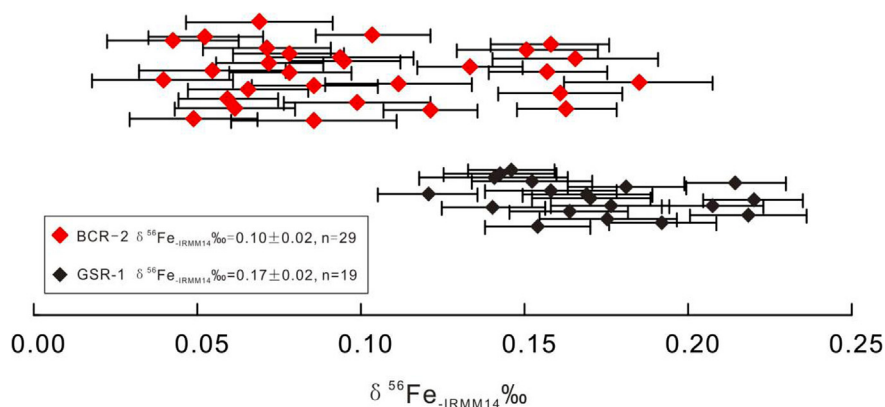

Fig. A. Fe isotope measurements of reference standards BCR-2 and GSR-1.

Table B
Reference values for standards BCR-2 and GSR-1.

	$\delta^{56}Fe_{-IRMM14}$‰	2δ	$\delta^{57}Fe_{-IRMM14}$‰	2δ	
GSR-1	0.17	0.02	0.26	0.03	Craddock and Dauphas (2011)
	0.17	0.04	0.24	0.05	Poitrasson and Freydier (2005)
BCR-2	0.09	0.01	0.13	0.02	Craddock and Dauphas (2011)
	0.08	0.13	0.14	0.22	Sharma et al. (2001)
	0.05	0.08	0.16	0.21	Dauphas et al. (2004)
	0.08	0.04			Weyer et al. (2005)
	0.09	0.03	0.13	0.03	Dauphas et al. (2009)

Table C
Fe isotope data for in-house solution standard ZXK.Fe-115.

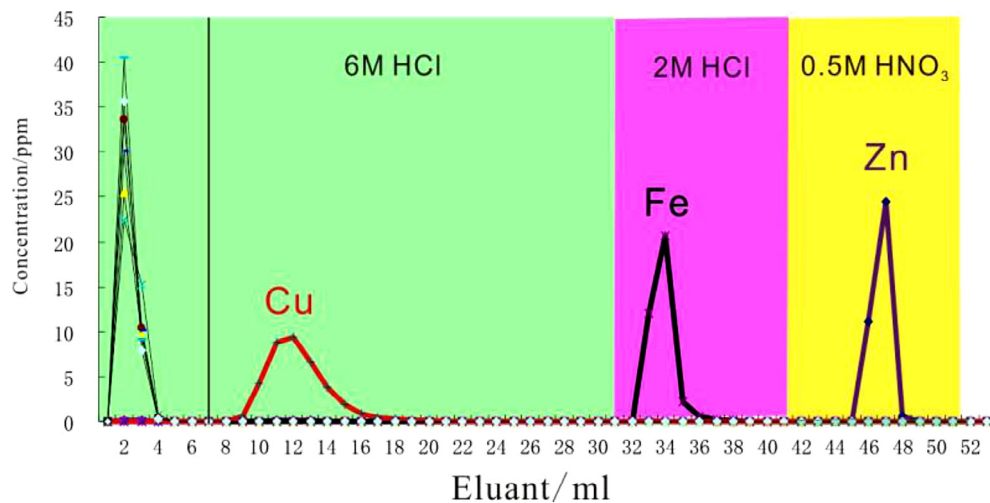|	$\delta^{56}Fe_{-IRMM14}$‰	2δ	$\delta^{57}Fe_{-IRMM14}$‰	2δ
ZXK.Fe115	0.83	0.04	1.21	0.07
	0.84	0.04	1.25	0.06
	0.86	0.03	1.23	0.06
	0.82	0.03	1.17	0.06
	0.85	0.03	1.24	0.07
	0.85	0.03	1.20	0.06
	0.82	0.04	1.19	0.07
	0.82	0.03	1.23	0.06
	0.81	0.03	1.21	0.06
	0.83	0.03	1.19	0.06
	0.84	0.03	1.18	0.06
Average	0.83		1.21	
SD	0.02		0.03	
2δ	0.01		0.02	
Recommended results by ZXK	0.84 ± 0.03		1.23 ± 0.05	

Fig. B. Elution curves of Cu-Fe-Zn (Zhu et al., 2015). [*] This elution curve is conducted with a mixing standard, not BCR-2.

although it may relate to f_{O2} in the ore-forming fluid. The present study suggests that the lighter Fe isotope is leached from granite during K-feldspar alteration leaving the altered granite enriched in the heavier Fe isotope, emphasizing major differences in alteration processes in the different ore types.

Alteration styles in orogenic gold deposits resemble those in porphyry deposits more closely than skarns. Mixing of Fe isotope signatures between those of igneous rocks and wall rock end-members has been demonstrated from the center to the rim of the Grasberg porphyry Cu-Au deposit, Indonesia (Graham et al., 2004). Such an

Table D
Former and *Later* solutions normalized to the eluted Fe from 31 to 40 ml as 100%.

Name[a]	*Former* 0-30 ml	Fe 31-40 ml	*Later* 41-50 ml	Yield
BCR-2A 10mg	0.01%	100%	0.08%	99.92%
BCR-2B 10mg	0.00%	100%	0.14%	99.85%

[a] Both BCR-2 standards were weighed as 10 mg. Iron concentrations of the three Fe solutions were scanned with Neptune *plus*. We can use ^{56}Fe intensity to infer the relative concentration of iron, although we could not obtain a precise Fe concentration of each solution.

explanation is clearly not applicable to the present study. The wall rock to the gold deposits is granite, and neither the basement nor the granite can cover the variation in Fe isotope composition displayed by the ores. The large Fe isotope variation shown by the ores in this study could relate to Rayleigh fractionation. The Fe isotope composition of the ore-forming fluid is inferred to be −0.37‰ to −0.53‰ (see above), a composition very similar to other studies (Beard et al., 2003a). Although it is hard to trace the source of Fe with such a value, Fe leached from the K-feldspar altered granite must have contributed at least part of the Fe. Basement rock may also supply part of the Fe via fluid-rock interaction. The average TFe_2O_3 content of the basement rocks may exceed 10 wt% but is <1 wt% in granite. Given such a difference, it is to be expected that no significant Fe isotope variation could be observed in the basement rock unlike in the K-feldspar altered granite.

7. CONCLUSIONS AND OUTLOOKS

Potassic-feldspar alteration is a widespread style of alteration resulting from fluid-rock interaction which can be associated with a broad range of hydrothermal ore-forming systems, notably in porphyry systems. The lower Fe content in granite relative to basaltic/mafic magma makes Fe isotopes in porphyries much more sensitive to the fluid-rock interaction process, and thus, Fe isotope variation in the K-feldspar alteration zone is a potential geothermometer (Fig. 7), which could also be further applied to other hydrothermal systems. At present there are limitations, however, particularly with respect to the complex analytical and sample procedures required, e.g., a combination of whole rock analysis (to measure total Fe) and Fe isotopic analysis. Furthermore, the presence of mineralization, especially pyrite, within the K-feldspar alteration halo could significantly affect the Fe component and the Fe isotope signature of the whole rock, and should be avoided when sampling; identification of the residual Fe-bearing minerals would be a pre-requisite before analysis. Despite these limitations, the large Fe-isotopic variation in the K-feldspar alteration zone has minimal impact on analytical uncertainties for the final temperature, which represents a potential geothermometer for the ore-forming systems.

The spatial distribution of Fe isotope compositions within the alteration zone is also an indicator of degree of alteration, and could thus be used in a vector approach to imply the direction of the orebody. In an ore-forming system, Fe isotopes behave differently in different ore zones. Enrichment in the light Fe isotope may sometimes imply termination of the mineralizing event in analogous sulfide-dominated deposits, a phenomenon which is meaningful for exploration. Although it is hard to trace the source of Fe only with a single Fe isotope analysis, Fe isotopes certainly could provide, in conjunction with other data, information on Fe source(s).

APPENDIX A

A.1. Part 1: checking of international rock standards

The results of international standards BCR-2 and GSR-1 have been listed in Table A and are depicted in Fig. A. The average value of $\delta^{56}Fe_{-IRMM14}$ for BCR-2 in our laboratory is 0.10 ± 0.02‰ ($n = 29$) and GSR-1 is 0.17 ± 0.02‰ ($n = 19$). This is coincident with previous studies (Table B). 2δ represents two standard error in both Tables A and B, which is calculated from the instrumental standard error of the $^{56}Fe/^{54}Fe$ or $^{57}Fe/^{54}Fe$ ratios. SD represents one standard deviation.

A.2. Part 2: checking of solution standards

An in-house solution standard, ZXK.Fe-115, provided by Prof. Xiang-Kun Zhu has been checked in our laboratory. $\delta^{56}Fe_{-IRMM14}$ of ZXK.Fe-115 is 0.83 ± 0.01‰ ($n = 11$, Table C). This value is very close to his recommended value of 0.84 ± 0.03‰.

A.3. Part 3: checking of yield

The purification follows a chemical procedure (Zhu et al., 2015) revised from Maréchal (1999) (Fig. B). Iron is eluted from 31 to 40 ml with 2M HCl. We have checked the eluted solution from 1 to 30 ml (this is termed *Former*) and the solution from 42 to 50 ml (this is termed *Later*) to see how much Fe has been lost (Table D). The yield of Fe is shown to be nearly 100%.

Additional references

Craddock P. R. and Dauphas N. (2011) Iron isotopic compositions of geological reference materials and chondrites. Geostandards Geoanal. Res. 35, 101–123.

Dauphas N., Janney P. E., Mendybaev R. A., Wadhwa M., Richter F. M., Davis A. M., van Zuilen M., Hines R. and Foley C. N. (2004) Chromatographic separation and multicollection-ICP-MS analysis of iron: investigating mass-dependent and independent isotope effects. Anal. Chem., 76, 5855–5863.

Dauphas N., Craddock P. R., Asimow P. D., Bennett V. C., Nutman A. P., and Ohnenstetter D. (2009) Iron isotopes may reveal the redox conditions of mantle melting from Archean to Present. Earth Planet Sci. Lett. 288, 255–267.

Maréchal C. N., Telouk P. and Albarede F. (1999) Precise analysis of copper and zinc isotopic compositions by plasma-source mass spectrometry. Chem. Geol. 156, 251–273.

Poitrasson F. and Freydier R. (2005) Heavy iron isotope composition of granites determined by high resolution MC-ICP-MS. Chem. Geol. 222, 132–147.

Sharma M., Polizzotto M. and Anbar A. D. (2001) Iron isotopes in hot springs along the Juan de Fuca Ridge. Earth Planet Sci. Lett. 194, 39–51.

Weyer S., Anbar A. D., Brey G. P., Münker C., Mezger K., and Woodland A. B. (2005) Iron isotope fractionation during planetary differentiation. Earth Planet Sci. Lett. 240, 251–264.

Zhu Z. Y., Jiang S. Y., Yang T. and Wei H. (2015) Improvements in Cu–Zn isotope analysis with MC-ICP-MS: a revisit of chemical purification, mass spectrometry measurement and mechanism of Cu/Zn mass bias decoupling effect. Int. J. Mass Spectrometry 393, 34–40.

REFERENCES

Armbrust G. A., Oyarzún J. and Arias J. (1977) Rubidium as a guide to ore in Chilean porphyry copper deposits. *Econ. Geol.* **72**, 1086–1100.

Anbar A. D., Jarzecki A. A. and Spiro T. G. (2005) Theoretical investigation of iron isotope fractionation between $Fe(H_2O)_6^{3+}$ and $Fe(H_2O)_6^{2+}$: implications for iron stable isotope geochemistry. *Geochim. Cosmochim. Acta* **69**, 825–837.

Archer C. and Vance D. (2006) Coupled Fe and S isotope evidence for Archean microbial Fe (III) and sulfate reduction. *Geology* **34**, 153–156.

Beard B. L., Handler R. M., Scherer M. M., Wu L., Czaja A. D., Heimann A. and Johnson C. M. (2010) Iron isotope fractionation between aqueous ferrous iron and goethite. *Earth Planet. Sci. Lett.* **295**, 241–250.

Beard B. L., Johnson C. M., Damm Von K. L. and Poulson R. L. (2003a) Iron isotope constraints on Fe cycling and mass balance in oxygenated Earth oceans. *Geology* **31**, 629–632.

Beard B. L., Johnson C. M., Skulan J. L., Nealson K. H., Cox L. and Sun H. (2003b) Application of Fe isotopes to tracing the geochemical and biological cycling of Fe. *Chem. Geol.* **195**, 87–117.

Bilenker L. D., VanTongeren J. A., Lundstrom C. C. and Simon A. C. (2017) Iron isotopic evolution during fractional crystallization of the uppermost Bushveld Complex layered mafic intrusion. *Geochem. Geophys. Geosyst.* **18**, 956–972.

Blanchard M., Poitrasson F., Méheut M., Lazzeri M., Mauri F. and Balan E. (2009) Iron isotope fractionation between pyrite (FeS_2), hematite (Fe_2O_3) and siderite ($FeCO_3$): a first-principles density functional theory study. *Geochim. Cosmochim. Acta* **73**, 6565–6578.

Bullen T. D., White A. F., Childs C. W., Vivit D. V. and Schulz M. S. (2001) Demonstration of significant abiotic iron isotope fractionation. *Geology* **29**, 699–702.

Butler I. B., Archer C., Vance D., Oldroyd A. and Rickard D. (2005) Fe isotope fractionation on FeS formation in ambient aqueous solution. *Earth Planet. Sci. Lett.* **236**, 430–442.

Chang Z., Large R. R. and Maslennikov V. (2008) Sulfur isotopes in sediment-hosted orogenic gold deposits: evidence for an early timing and a seawater sulfur source. *Geology* **36**, 971–974.

Chen G. Y., Shao W. and Sun D. S. (1989) *Genetic Mineralogy of Gold Deposits in Jiaodong Region with Emphasis on Gold Prospecting*. Chongqing Publishing House, Chongqing.

Chen L.-M., Song X.-Y., Zhu X.-K., Zhang X.-Q., Yu S.-Y. and Yi J.-N. (2013) Iron isotope fractionation during crystallization and sub-solidus re-equilibration: constraints from the Baima mafic layered intrusion, SW China. *Chem. Geol.* **380**, 97–109.

Chen Y. J. (2006) Orogenic-type deposits and their metallogenic model and exploration potential. *Geol. China* **33**, 1181–1196.

Cooke D. R., Mcphail D. C. and Bloom M. S. (1996) Epithermal glold mineralization, Acupan, Baguio District, Philippines: geology, mineralization, alteration, and the thermochemical environment of ore deposition. *Econ. Geol.* **91**, 243–272.

Crerar D. A., Susak N. J., Borcsik M. and Schwartz S. (1978) Solubility of the buffer assemblage pyrite + pyrrhotite + magnetite in NaCl solutions from 200 to 350 C. *Geochim. Cosmochim. Acta* **42**, 1427–1437.

Fan H.-R., Zhai M. G., Xie Y. H. and Yang J.-H. (2003) Ore-forming fluids associated with granite-hosted gold mineralization at the Sanshandao deposit, Jiaodong gold province, China. *Miner. Deposita* **38**, 739–750.

Fantle M. S. and DePaolo D. J. (2004) Iron isotopic fractionation during continental weathering. *Earth Planet. Sci. Lett.* **228**, 547–562.

Foden J., Sossi P. A. and Wawryk C. M. (2015) Fe isotopes and the contrasting petrogenesis of A-, I- and S-type granite. *Lithos* **212–215**, 32–44.

Frierdich A. J., Beard B. L., Reddy T. R., Scherer M. M. and Johnson C. M. (2014a) Iron isotope fractionation between aqueous Fe(II) and goethite revisited: New insights based on a multi-direction approach to equilibrium and isotopic exchange rate modification. *Geochim. Cosmochim. Acta* **139**, 383–398.

Frierdich A. J., Beard B. L., Scherer M. M. and Johnson C. M. (2014b) Determination of the Fe(II)aq–magnetite equilibrium iron isotope fractionation factor using the three-isotope method and a multi-direction approach to equilibrium. *Earth Planet. Sci. Lett.* **391**, 77–86.

Gagnevin D., Boyce A. J., Barrie C. D., Menuge J. F. and Blakeman R. J. (2012) Zn, Fe and S isotope fractionation in a large hydrothermal system. *Geochim. Cosmochim. Acta* **88**, 183–198.

Gao J. F., Lu J. J., Lai M. Y., Lin Y. P. and Pu W. (2003) Analysis of trace elements in rock samples using HR-ICPMS. *J. Nanjing University (Nat. Sci.)* **39**, 844–850.

Gao Z., Zhu X., Sun J., Luo Z., Bao C., Tang C. and Ma J. (2017) Spatial evolution of Zn-Fe-Pb isotopes of sphalerite within a single ore body: a case study from the Dongshengmiao ore deposit, Inner Mongolia, China. *Miner. Deposita* **15**, 1–11.

Goldfarb R. J., Groves D. I. and Gardoll S. (2001) Orogenic gold and geologic time: a global synthesis. *Ore Geol. Rev.* **18**, 1–75.

Goodfellow W. D., Lydon J. W. and Turner R. (1993) Geology and genesis of stratiform sediment-hosted (SEDEX) zinc-lead-silver sulphide deposits. *Geol. Assoc. Can. Spec. Pap.* **40**, 1–25.

Graham S., Pearson N., Jackson S., Griffin W. and O'Reilly S. Y. (2004) Tracing Cu and Fe from source to porphyry: in situ determination of Cu and Fe isotope ratios in sulfides from the Grasberg Cu–Au deposit. *Chem. Geol.* **207**, 147–169.

Groves D. I., Goldfarb R. J. and Gebre-Mariam M. (1998) Orogenic gold deposits: a proposed classification in the context of their crustal distribution and relationship to other gold deposit types. *Ore Geol. Rev.* **13**, 7–27.

Guilbaud R., Butler I. B., Ellam R. M., Rickard D. and Oldroyd A. (2011) Experimental determination of the equilibrium Fe isotope fractionation between and FeSm (mackinawite) at 25 and 2 °C. *Geochim. Cosmochim. Acta* **75**, 2721–2734.

Heimann A., Beard B. L. and Johnson C. M. (2008) The role of volatile exsolution and sub-solidus fluid/rock interactions in producing high $^{56}Fe/^{54}Fe$ ratios in siliceous igneous rocks. *Geochim. Cosmochim. Acta* **72**, 4379–4396.

Hou M.-L., Jiang S.-Y., Jiang Y.-H. and Ling H.-Fei L. (2006) S-Pb isotope geochemistry and Rb-Sr geochronology of the Penglai gold field in the eastern Shangdong province. *Acta Petrologica Sinica* **22**, 2525–2533.

Hou M.-L., Jiang Y.-H., Jiang S.-Y., Ling H.-F. and Zhao K.-D. (2007) Contrasting origins of late Mesozoic adakitic granitoids from the northwestern Jiaodong Peninsula, east China: implications for crustal thickening to delamination. *Geol. Mag.* **144**, 619–631.

Huston D. L. (1999) Stable isotopes and their significance for understanding the genesis of volcanic-hosted massive sulfide deposits: a review. *Rev. Econ. Geol.* **8**, 157–179.

Jahn B., Cornichet J., Cong B. and Yui T. F. (1996) Ultrahigh-eNd eclogites from an ultrahigh-pressure metamorphic terrane of China. *Chem. Geol.* **127**, 61–79.

Jahn B., Liu D., Wan Y., Song B. and Wu J. (2008) Archean crustal evolution of the Jiaodong Peninsula, China, as revealed by zircon SHRIMP geochronology, elemental and Nd-isotope geochemistry. *Am. J. Sci.* **308**, 232–269.

Jiang S. Y., Dai B. Z., Jiang Y. H., Zhao H. X. and Hou M. N. (2009) Jiaodong and Xiaoqinling: two orogenic gold provinces formed in different tectonic settings. *Acta Petrologica Sinica* **25**, 2727–2738.

Johnson C. M., Beard B. L., Beukes N. J., Klein C. and O'Leary J. M. (2003) Ancient geochemical cycling in the Earth as inferred from Fe isotope studies of banded iron formations from the Transvaal Craton. *Contrib. Miner. Petrol.* **144**, 523–547.

Johnson C. M., Skulan J. L., Beard B. L. and Sun H. (2002) Isotopic fractionation between Fe (III) and Fe (II) in aqueous solutions. *Earth Planet. Sci. Lett.* **195**, 141–153.

Li W., Jackson S. E., Pearson N. J. and Graham S. (2010) Copper isotopic zonation in the Northparkes porphyry Cu–Au deposit, SE Australia. *Geochim. Cosmochim. Acta* **74**, 4078–4096.

Li Z.-X. (1994) Collision between the North and South China blocks: a crustal-detachment model for suturing in the region east of the Tanlu fault. *Geology* **22**, 739–742.

Liu B. and Shen K. (1999) *Thermodynamics of Fluid Inclusions*. Geological Publishing House, Beijing.

Lu H. Z., Guha J. and Fang G. B. (1999) Characteristics of ore-forming fluid in Linglong gold mine, Shandong, China. *Geochimica* **28**, 421–437.

Lü G. and Kong Q. (1993) *Geology of Linglong-Jiaojia Type of Gold Deposits in Jiaodong Area*. Science Press, Beijing.

Ma L., Jiang S.-Y., Dai B.-Z., Jiang Y.-H., Hou M.-L., Pu W. and Xu B. (2013) Multiple sources for the origin of Late Jurassic Linglong adakitic granite in the Shandong Peninsula, eastern China: Zircon U-Pb geochronological, geochemical and Sr–Nd–Hf isotopic evidence. *Lithos* **162–163**, 251–263.

Ma L., Jiang S.-Y., Hofmann A. W., Dai B.-Z., Hou M.-L., Zhao K.-D., Chen L.-H., Li J.-W. and Jiang Y.-H. (2014) Lithospheric and asthenospheric sources of lamprophyres in the Jiaodong Peninsula: a consequence of rapid lithospheric thinning beneath the North China Craton? *Geochim. Cosmochim. Acta* **124**, 250–271.

Maher K. C. and Larson P. B. (2007) Variation in copper isotope ratios and controls on fractionation in hypogene skarn mineralization at Coroccohuayco and Tintaya, Perú. *Econ. Geol.* **102**, 225–237.

Mao J., Wang Y., Li H., Pirajno F., Zhang C. and Wang R. (2008) The relationship of mantle-derived fluids to gold metallogenesis in the Jiaodong Peninsula: evidence from D–O–C–S isotope systematics. *Ore Geol. Rev.* **33**, 361–381.

Maréchal C. N., Télouk P. and Albarède F. (1999) Precise analysis of copper and zinc isotopic compositions by plasma-source mass spectrometry. *Chem. Geol.* **156**, 251–271.

Markl G., Blanckenburg von F. and Wagner T. (2006) Iron isotope fractionation during hydrothermal ore deposition and alteration. *Geochim. Cosmochim. Acta* **70**, 3011–3030.

Maruyama S., Isozaki Y., Kimura G. and Terabayashi M. (1997) Paleogeographic maps of the Japanese Islands: plate tectonic synthesis from 750 Ma to the present. *Island Arc* **6**, 121–142.

Mathur R., Titley S., Barra F., Brantley S., Wilson M., Phillips A., Munizaga F., Maksaev V., Vervoort J. and Hart G. (2009) Exploration potential of Cu isotope fractionation in porphyry copper deposits. *J. Geochem. Explor.* **102**, 1–6.

Mineev S. D., Polyakov V. B. and Permyakov Y. V. (2007) Equilibrium iron isotope fractionation factors for magnetite from Mössbauer spectroscopy and inelastic nuclear resonant X-ray scattering data. *Geochim. Cosmochim. Acta* **71**, A669.

Ohmoto H. (1972) Systematics of sulfur and carbon isotopes in hydrothermal ore deposits. *Econ. Geol.* **67**, 551–578.

Poitrasson F. and Freydier R. (2005) Heavy iron isotope composition of granites determined by high resolution MC-ICP-MS. *Chem. Geol.* **222**, 132–147.

Polyakov V. B. and Mineev S. D. (2000) The use of Mössbauer spectroscopy in stable isotope geochemistry. *Geochim. Cosmochim. Acta* **64**, 849–865.

Polyakov V. B. and Soultanov D. M. (2011) New data on equilibrium iron isotope fractionation among sulfides: constraints on mechanisms of sulfide formation in hydrothermal and igneous systems. *Geochim. Cosmochim. Acta* **75**, 1957–1974.

Polyakov V. B., Clayton R. N., Horita J. and Mineev S. D. (2007) Equilibrium iron isotope fractionation factors of minerals: reevaluation from the data of nuclear inelastic resonant X-ray scattering and Mössbauer spectroscopy. *Geochim. Cosmochim. Acta* **71**, 3833–3846.

Qiu Y., Groves D. I., McNaughton N. J., Wang L.-G. and Zhou T. (2002) Nature, age, and tectonic setting of granitoid-hosted, orogenic gold deposits of the Jiaodong Peninsula, eastern North China craton, China. *Miner. Deposita* **37**, 283–305.

Rickard D. (1995) Kinetics of FeS precipitation: Part 1. Competing reaction mechanisms. *Geochim. Cosmochim. Acta* **59**, 4367–4379.

Robinson B. W. and Kusakabe M. (1975) Quantitative preparation of sulfur dioxide, for $^{34}S/^{32}S$ analyses, from sulfides by combustion with cuprous oxide. *Anal. Chem.* **47**, 1179–1181.

Rouxel O., Shanks W. C., Bach W. and Edwards K. (2008) Integrated Fe- and S-isotope study of seafloor hydrothermal vents at East Pacific Rise 9–10 N. *Chem. Geol.* **252**, 214–227.

Rustad J. R., Casey W. H., Yin Q.-Z., Bylaska E. J., Felmy A. R., Bogatko S. A., Jackson V. E. and Dixon D. A. (2010) Isotopic

fractionation of Mg^{2+}(aq), Ca^{2+}(aq), and Fe^{2+}(aq) with carbonate minerals. *Geochim. Cosmochim. Acta* **74**, 6301–6323.

Saunier G., Pokrovski G. S. and Poitrasson F. (2011) First experimental determination of iron isotope fractionation between hematite and aqueous solution at hydrothermal conditions. *Geochim. Cosmochim. Acta* **75**, 6629–6654.

Sangster D. F. (1968) Relative sulphur isotope abundances of ancient seas and strata-bound sulphide deposits. *Proc. Geol. Assoc. Can.* **17**, 79–91.

Schauble E. A., Rossman G. R. and Taylor H. P. (2001) Theoretical estimates of equilibrium Fe-isotope fractionations from vibrational spectroscopy. *Geochim. Cosmochim. Acta* **65**, 2487–2497.

Schuessler J. A., Schoenberg R. and Sigmarsson O. (2009) Iron and lithium isotope systematics of the Hekla volcano, Iceland—evidence for Fe isotope fractionation during magma differentiation. *Chem. Geol.* **258**, 78–91.

Schuessler J. A., Schoenberg R., Behrens H. and Blanckenburg F. V. (2007) The experimental calibration of the iron isotope fractionation factor between pyrrhotite and peralkaline rhyolitic melt. *Geochim. Cosmochim. Acta* **71**, 417–433.

Sharma M., Polizzotto M. and Anbar A. D. (2001) Iron isotopes in hot springs along the Juan de Fuca Ridge. *Earth Planet. Sci. Lett.* **194**, 39–51.

Shen K., Hu S. X., Sun J. G., Ling H. F., Zhao Y. Y. and Sun M. Z. (2000) Characteristics of ore-forming fluids of the Dayingezhuang gold deposit in Eastern Shandong, China. *Acta Petrologica Sinica* **16**, 542–550.

Skulan J. L., Beard B. L. and Johnson C. M. (2002) Kinetic and equilibrium Fe isotope fractionation between aqueous Fe (III) and hematite. *Geochim. Cosmochim. Acta* **66**, 2995–3015.

Sossi P. A., Foden J. D. and Halverson G. P. (2012) Redox-controlled iron isotope fractionation during magmatic differentiation: an example from the Red Hill intrusion, S. *Tasmania. Contribut. Mineral. Petrol.* **164**, 757–772.

Tang J., Zheng Y.-F., Wu Y.-B., Gong B. and Liu X. (2007) Geochronology and geochemistry of metamorphic rocks in the Jiaobei terrane: constraints on its tectonic affinity in the Sulu orogen. *Precambr. Res.* **152**, 48–82.

Teng F.-Z., Dauphas N. and Helz R. T. (2008) Iron isotope fractionation during magmatic differentiation in Kilauea Iki Lava Lake. *Science* **320**, 1620–1622.

Wang H. and Salveson I. (2005) A review on the mineral chemistry of the non-stoichiometric iron sulphide, $Fe_{1-x}S$ ($0 \le x \le 0.125$): polymorphs, phase relations and transitions, electronic and magnetic structures. *Phase Transitions* **78**, 547–567.

Ulrich T. and Heinrich C. A. (2002) Geology and alteration geochemistry of the porphyry Cu-Au deposit at Bajo de la Alumbrera, Argentina. *Eonomic Geol.* **97**, 1865–1888.

Wang S. X., Zhu X. and Song X. Y. (2012) Fe Isotopic characteristics of V-Ti magnetite deposit in panzhihua area of sichuan province and their genetic implications. *Acta Geoscientica Sinica* **33**, 995–1004 (In Chinese with English abstract).

Wang Y., Zhu F. and Gong R. (2002) Tectonic isotope geochemistry – further study on sulphur isotope of Jiaodong Gold Concentration Area. *Gold* **4**, 1–16 (In Chinese with English abstract).

Wang Y., Zhu X.-K. and Cheng Y. (2015) Fe isotope behaviours during sulfide-dominated skarn-type mineralisation. *J. Asian Earth Sci.* **103**, 374–392.

Wang Y., Zhu X.-K., Mao J.-W., Li Z.-H. and Cheng Y.-B. (2011) Iron isotope fractionation during skarn-type metallogeny: a case study of Xinqiao Cu–S–Fe–Au deposit in the Middle-Lower Yangtze valley. *Ore Geol. Rev.* **43**, 194–202.

Wawryk C. M. and Foden J. D. (2015) Fe-isotope fractionation in magmatic-hydrothermal mineral deposits: a case study from the Renison Sn-W deposit, Tasmania. *Geochim. Cosmochim. Acta* **150**, 285–298.

Welch S. A., Beard B. L., Johnson C. M. and Braterman P. S. (2003) Kinetic and equilibrium Fe isotope fractionation between aqueous Fe(II) and Fe(III). *Geochim. Cosmochim. Acta* **67**, 4231–4250.

Wiesli R. A., Beard B. L. and Johnson C. M. (2004) Experimental determination of Fe isotope fractionation between aqueous Fe (II), siderite and "green rust" in abiotic systems. *Chem. Geol.* **211**, 343–362.

Xu J. H., He Z. L. and Xie Y. L. (1996) *Geochemistry of Ore-Forming Fluids of Gold Deposits in Greenstone Belt*. Geological Publishing House, Beijing.

Yang J.-H. and Zhou X.-H. (2001) Rb-Sr, Sm-Nd, and Pb isotope systematics of pyrite: implications for the age and genesis of lode gold deposits. *Geology* **29**, 711–714.

Yang L., Deng J., Guo C., Zhang J., Jiang S., Gao B., Gong Q. and Wang Q. (2009) Ore-forming fluid characteristics of the Dayingezhuang gold deposit, Jiaodong gold province, China. *Resource Geol.* **59**, 181–193.

Yang L.-Q., Deng J., Goldfarb R. J., Zhang J., Gao B.-F. and Wang Z.-L. (2014) $^{40}Ar/^{39}Ar$ geochronological constraints on the formation of the Dayingezhuang gold deposit: new implications for timing and duration of hydrothermal activity in the Jiaodong gold province, China. *Gondwana Res.* **25**, 1469–1483.

Ying H. (1994) Isotopic compositions and their geological significance of Jingqingding and Denggezhuang gold deposits, Jiaodong. *J. Precious Metallic Geol.* **3**, 201–207.

Zhai M., Yang J. and Liu W. (2001) Large clusters of gold deposits and large-scale metallogenesis in the Jiaodong Peninsula, Eastern China. *Sci. China Ser. D-Earth Sci.* **44**, 758–768.

Zhang H.-F., Sun M., Zhou X.-H., Zhou M.-F., Fan W.-M. and Zheng J.-P. (2003) Secular evolution of the lithosphere beneath the eastern North China Craton: evidence from Mesozoic basalts and high-Mg andesites. *Geochim. Cosmochim. Acta* **67**, 4373–4387.

Zheng Y. (2008) A perspective view on ultrahigh-pressure metamorphism and continental collision in the Dabie-Sulu orogenic belt. *Chin. Sci. Bull.* **53**, 3081–3104.

Zhou X. M. and Li W. X. (2000) Origin of Late Mesozoic igneous rocks in Southeastern China: implications for lithosphere subduction and underplating of mafic magmas. *Tectonophysics* **326**, 269–287.

Zhu B., Zhang H.-F., Zhao X.-M. and He Y.-S. (2016) Iron isotope fractionation during skarn-type alteration: implications for metal source in the Han-Xing iron skarn deposit. *Ore Geol. Rev.* **74**, 139–150.

Zhu X. (2000) Secular variation of iron isotopes in North Atlantic Deep Water. *Science* **287**, 2000–2002.

Zhu X. K., Guo Y., O'Nions R. K., Young E. D. and Ash R. D. (2001) Isotopic homogeneity of iron in the early solar nebula. *Nature* **412**, 311–313.

Zhu X. K., O'Nions R. K., Guo Y., Belshaw N. S. and Rickard D. (2000) Determination of natural Cu-isotope variation by plasma-source mass spectrometry: implications for use as geochemical tracers. *Chem. Geol.* **163**, 139–149.

Zhu Z.-Y., Jiang S.-Y., Yang T. and Wei H.-Z. (2015) Improvements in Cu–Zn isotope analysis with MC-ICP-MS: a revisit of chemical purification, mass spectrometry measurement and mechanism of Cu/Zn mass bias decoupling effect. *Int. J. Mass Spectrom.* **393**, 34–40.

Associate Editor: Weidong Sun